

MATERIALS CHEMISTRY

Lehrstuhl für Werkstoffchemie

Rheinisch-Westfälische Technische Hochschule Aachen

Prof. Jochen M. Schneider, Ph. D.

Pascal Bliem

Oxygen induced change in binding energies in metal boride systems

Supervisors:

Prof. Jochen M. Schneider, Ph. D.

Oliver Hunold, M. Sc.

Abstract in English

Metal borides exhibit interesting properties making them suitable for a wide range of applications. Yet no comparative oxidation study on metal borides is present in literature. In this work, the oxygen induced change in binding energies (chemical shift) is utilized to determine the buildup of oxide layers on metal borides with varying boron content via X-ray photoelectron spectroscopy (XPS). Literature on binding energies in metal boride systems is rather meagre and partially exhibits large scattering of reported values. Binding energies of AlB_2 , CaB_6 , MgB_2 , TiB_2 , VB_2 , YB_6 , ZrB_2 , AlYB_{14} and ZrYB_{14} were measured with XPS. Structural composition was probed by X-ray diffraction. It was found that samples with high phase impurities exhibit large deviations from literature values. This emphasizes the major influence of phase impurities on measured binding energies. Measured B 1s binding energies of metal diborides spread within a range of 1.2 eV, while AlYB_{14} and ZrYB_{14} exhibit identical values for each B 1s and Y 3d binding energies. This suggests that, with increasing boron content, the electronic structure is predominantly dictated by the boron framework. Samples of TiB_2 , AlB_2 , CaB_6 , AlYB_{14} and ZrYB_{14} were oxidized. XPS depth profiles of the oxide layers revealed that AlYB_{14} and ZrYB_{14} oxidized less than TiB_2 and AlB_2 , which may be attributed to the strongly bonded icosahedral boron framework of AlYB_{14} and ZrYB_{14} that limits the accessibility of both boron and metals. In TiB_2 , AlB_2 , AlYB_{14} and ZrYB_{14} , boron is relatively less oxidized than metal. This may be ascribed to the higher strength of B-B bonds compared to M-B and M-M bonds. These observations are approved by estimated values of the oxide layers' thickness.

Abstract in German

Metallboride weisen interessante Eigenschaften auf, wodurch sie für ein großes Spektrum an Anwendungen geeignet sind. Bisher ist keine vergleichende Oxidationsstudie zu Metallboriden vorhanden. In dieser Arbeit wird die sauerstoffinduzierte Änderung der Bindungsenergien (chemische Verschiebung) verwendet um den Aufbau von Oxidschichten auf Metallboriden mit variierendem Borgehalt mittels Röntgenphotoelektronenspektroskopie (XPS) zu bestimmen. Literatur zu Bindungsenergien von Metallboridsystemen ist eher knapp und weist teilweise große Streuungen der berichteten Werte auf. Die Bindungsenergien von AlB_2 , CaB_6 , MgB_2 , TiB_2 , VB_2 , YB_6 , ZrB_2 , AlYB_{14} und ZrYB_{14} wurden mittels XPS gemessen. Die strukturelle Zusammensetzung wurde durch Röntgenbeugung untersucht. Es hat sich gezeigt, dass Proben mit hohen Phasenunreinheiten stark von Literaturwerten abweichen. Dies hebt den wesentlichen Einfluss von Phasenunreinheiten auf gemessene Bindungsenergien hervor. Gemessene B 1s Bindungsenergien von Metaldiboriden erstrecken sich über eine Spanne von 1.2 eV, wohingegen AlYB_{14} und ZrYB_{14} jeweils identische Werte für B 1s und Y 3d Bindungsenergien aufweisen. Dies lässt vermuten, dass die elektronische Struktur mit zunehmendem Borgehalt von der Borstruktur bestimmt wird. Proben von TiB_2 , AlB_2 , CaB_6 , AlYB_{14} und ZrYB_{14} wurden oxidiert. XPS-Tiefenprofile der Oxidschichten offenbarten, dass AlYB_{14} und ZrYB_{14} weniger oxidierten als TiB_2 und AlB_2 . Dies könnte sich auf die stark gebundene, ikosaedrische Borstruktur von AlYB_{14} und ZrYB_{14} zurückführen lassen, welche die Zugänglichkeit von Bor und Metallen einschränkt. Bei TiB_2 , AlB_2 , AlYB_{14} und ZrYB_{14} ist Bor weniger oxidiert als das Metall. Dies könnte sich durch die stärkeren B-B Bindungen, verglichen mit M-B und M-M Bindungen, begründen lassen. Abgeschätzte Werte für die Dicken der Oxidschichten bestätigen diese Beobachtungen.

Table of Contents

1. Introduction.....	1
2. Review	2
2.1 Structure, properties and applications of metal borides	2
2.2 Oxidation behavior of metal borides.....	5
2.3 Bonding of metal borides	6
3. Methods	7
3.1 Sample preparation	7
3.1.1 High power pulsed magnetron sputtering (HPPMS)	7
3.1.2 Sintering	7
3.2 Characterization	8
3.2.1 Laser microscopy	8
3.2.2 Energy dispersive X-ray analysis (EDX).....	8
3.2.3 X-ray diffraction (XRD)	9
3.2.4 X-ray photoelectron spectroscopy (XPS)	10
4. Results and discussion.....	11
5. Conclusion	27
6. Future work	28
7. Acknowledgements.....	29
8. Appendix 1.....	29
9. Appendix 2.....	34
10. References.....	36

1. Introduction

Metal borides exhibit a variety of structures that are substantially determined by their boron content [1]. They are used in a wide range of applications due to properties like high melting points, high hardness, chemical inertness and often good thermal and electrical conductivity [2, 3]. To guarantee an optimal usage of metal boride materials, it is crucial to understand the oxidation behavior of these compounds. In microelectronic applications, where metal borides are used as barrier layers [4] and interconnects in ultra-large-scale integrated circuits [5], already low degrees of oxidation can affect the material's performance. For example it is supposed that oxide coating in grain boundaries of TiB_2 films cause electron scattering and thereby increases the resistivity [5].

Some general influences on the oxidation behavior regarding structure [6] and bond strength [7] have been mentioned in literature. To the author's best knowledge, a comprehensive systematic study or review on the oxidation behaviors of a major selection of different metal borides is not present. Existing oxidation studies mainly focus on oxidation kinetics and weight gain of certain compounds. Especially initial stages of oxidation have not been studied so far. To investigate the buildup of very thin oxide layers, surface sensitive analysis techniques like X-ray photoelectron spectroscopy (XPS) have to be used. Bonding with oxygen causes a chemical shift in the binding energies of an element's core shell electrons, which can be detected with XPS. Hence, the oxygen induced change in binding energies can be used to identify present compounds and therefore the composition of the oxide layer [8].

In this work, the buildup of thin oxide layers on metal borides with varying boron content and structure is comparatively investigated to gain information about early stages of oxidation. XPS in combination with Ar^+ ion etching is used to obtain depth profiles of the oxide layers and reconstruct their composition.

To clearly identify a compound via XPS it is crucial to have reliable literature values of binding energies. The available literature of binding energies in metal boride systems is rather meagre and exhibits partially large scattering. The absence of charge control in many publications might cause a

deviation of measured values. Hence, a strategy of this work is to obtain a consistently measured collection of binding energy values of a wide range of metal borides, provide a comparison with present literature and investigate their bonding.

2. Review

2.1 Structure, properties and applications of metal borides

It is known that boron predominantly forms covalent compounds with metals, where direct B-B interactions are evidently responsible for a wide range of possible structure types of metal borides. Several metals possess the ability to form different stable phases with boron resulting in a variety of compounds with significant variation in the B/M ratio, ranging from hemiborides to extremely boron rich phases like ZrB_{51} [9] or YB_{66} [10]. In these compounds, boron can form linear (M_2B , MB), planar/sheet-like (M_3B_4 , MB_2) or three-dimensional (MB_4 , MB_6 , MB_{12}) structures (see **Figure 1**) [1, 11].

Experimental [12-16] and theoretical [17] data suggest that stable transition metal monoborides appear in cubic NaCl structure (space group (SG): $Fm-3m$)(e.g. ZrB [12], HfB [13]), hexagonal WC structure (SG: $P6m2$)(e.g. RuB [14], OsB , IrB [15]) or hexagonal anti-NiAs structure (SG: $P6_3/mmc$)(e.g. RhB , PtB [16]) and that they are all metallic [17].

Common M_3B_4 -type metal borides crystallize in an orthorhombic structure (SG: $Immm$) [18] (e.g. Ta_3B_4 , Mn_3B_4 [3], Cr_3B_4 [3, 18], Re_3B_4 , Ru_3B_4 , Os_3B_4 [3]). This structure contains very short and directional covalent M-B and B-B bonds. The charge accumulation between M-B and B-B atoms results in exceptional high bulk moduli (~ 330 - 370 GPa) [18].

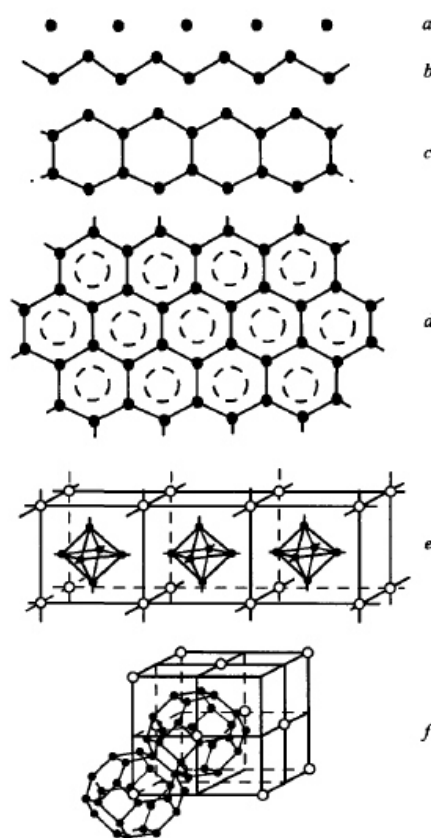


Figure 1: Possible configuration of boron in a) M_2B , b) MB , c) M_3B_4 , d) MB_2 , e) $MB_{4/6}$ and f) MB_{12} [1]

The metal's electronegativity plays an important role for the structure of metal diborides. Metals possessing a lower electronegativity than boron tend to donate electrons to vicinal boron atoms ($M^{2+}B_2^{2-}$). This favors the formation of graphite-like planar boron layers with hexagonal prismatic sites [19] and makes it isoelectronic with that of graphite [11], thereby the layer formation has been attributed to the formation of sp^2 configurations of the boron atoms [1]. This type is known as the hexagonal AlB_2 structure (SG: $P6/mmm$) (e.g. MgB_2 , ScB_2 , TiB_2 , VB_2 , CrB_2 , MnB_2 , ZrB_2 , NbB_2) [19]. The metal atoms' excess valence electrons are regarded as metallic, which explains the metallic optical and electric properties of many compounds [11]. In the case metal's electronegativity is higher than of boron, boron becomes an electron acceptor and favors to create puckered sheets. That contributes to a variety of possible structures, namely "puckered (boron sheet) ReB_2 -type (SG: $P6_3/mmc$), puckered OsB_2 -type (SG: $Pmmn$), planar-puckered MoB_2 -type (SG: $R-3m$) and WB_2 -type (SG: $P6_3/mmc$)" [20].

With increasing B/M ratio (>4), metal borides contain three-dimensional boron structures, mostly polyhedra (octahedron, cuboctahedron, icosahedron), that can be regarded as dianions ($B_{6/12}^{2-}$) [10, 11]. For octahedra there are 7 internal bonding orbitals (1 s -symmetry, 3 p -symmetry and 3 d -symmetry molecular orbitals), requiring 14 electrons plus 6 electrons for external bonding. For cuboctahedra and icosahedra there are 13 internal bonding orbitals (1 s -symmetry, 3 p -symmetry, 5 d -symmetry and 4 f -symmetry molecular orbitals), requiring 26 electrons plus 12 electrons for external bonding [11, 21]. Boron has three valence electrons, therefore a deficiency of two electrons per polyhedron has to be compensated by ionization of the metal component. Hence, rather electropositive metals tend to form compounds containing three dimensional boron structures [10, 11]. It is noteworthy that without an ideal spherical symmetry of the polyhedra the higher-lying orbitals split into several degenerated states, which locates the bonding charge in the centers of the polyhedral faces [21].

Both MB_4 and MB_6 type metal borides are reported to form boron octahedra, which are linked to adjacent octahedra by covalent B-B bonds [10, 11]. The MB_4 types contain single boron atoms that are bonded in pairs and are not part of an octahedron [11]. Metal tetraborides form a

variety of different crystal structures like orthorhombic *Immm* (CrB₄ [22]), orthorhombic *Pnnm* (CrB₄ [23], FeB₄ [24]), monoclinic *P2₁/c* (MnB₄ [25]) and hexagonal *P6₃/mmc* (WB₄, ReB₄, TcB₄ [26]). Common metal hexaborides appear in a CsCl-type simple cubic structure (SG: *Pm-3m*) [27] (e.g. YB₆, CaB₆ [27], LaB₆ [10]). Metal atoms are located in the center of a cube with octahedra at its edges and function as electron donators to the boron octahedra ($M^{2+}B_6^{2-}$) [21, 27].

Metal dodecaborides contain more complex boron polyhedra [11], namely cuboctahedra (e.g. YB₁₂ [10], ZrB₁₂ [11], UB₁₂ [28]) and icosahedra (e.g. α -AlB₁₂, γ -AlB₁₂ [29]). The electron deficiency of the B₁₂ units is, as mentioned before, compensated by charge transferring from the metal atoms ($M^{2+}B_{12}^{2-}$), which are located in the voids between the boron polyhedrons [11]. Cuboctahedra containing compounds usually form *fcc* structures (SG: *Fm-3m-O_h⁵*) similar to NaCl, occasionally also tetragonal structures (e.g. ScB₁₂ SG: *I4/mmm*), with strong covalent B-B bonds within and among the cuboctahedra. Therefore only metals with suitable ionic radii, comparable to interstitial voids, are known to form these compounds and the metal species has little influence on the lattice parameter [28]. Tetragonal α -AlB₁₂ (SG: *P4₁2₁2* or *P4₃2₁2*) and orthorhombic γ -AlB₁₂ (SG: *P2₁2₁2*) are interesting representatives of icosahedron containing dodecaborides, in which the boron framework consists of a combination of icosahedra and icosahedron containing B₂₀ units [29].

Furthermore, boron icosahedra are the main building blocks of M₂B₁₄ and ternary MMB₁₄ type compounds [10]. The latter will be emphasized in this work as they exhibit excellent properties making them suitable for various applications [30]. The icosahedra are reported to be arranged at the edges of a rhombohedron [21]. This might explain, why many of these compounds form orthorhombic structures such as *Imma* (e.g. AlYB₁₄ [30]) or *Imam* (e.g. AlLiB₁₄, AlMgB₁₄ [31]). Half of the icosahedral bonds link it to vicinal icosahedra while the other half is connected to isolated boron atoms. In this case, stabilization of the boron framework requires four electrons $[(M^{2+})_2(B_{12}^{2-})(B^-)_2]$ [10]. Transferring of too few or too much electrons decrease the stability of the boron framework, hence these ternary compounds are usually not stoichiometric. For example, the most stable stoichiometry for AlYB₁₄ has been calculated to actually be Al_{0.5}YB₁₄ [30].

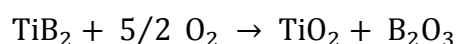
To sum up some of the discussions above, metal borides feature covalent B-B bonds that often are relatively short and highly directional, hence strong [1, 3, 17]. Excess metal valence electrons, which are not required to stabilize the boron framework, cause the metallic character of these compounds [11]. The strong bonding and metallic character in many metal borides lead to properties such as high melting points, thermal shock resistivity, high hardness, high incompressibility, chemical inertness and good thermal and electrical conductivity [2, 3]. Fields of application are space flight [3, 32], cutting tools, hard coatings, abrasive materials, refractory alloys [1, 3, 17, 30], microelectronics [4, 5, 33], electrodes [34, 35], beta-voltaic cells [21] and superconductors [36].

2.2 Oxidation behavior of metal borides

The compound structure seems to have a significant influence on the relative degree of oxidation. In mono- or diborides, boron forms one- or two-dimensional frameworks, which makes both metal and boron easily accessible. In contrast, in more boron-rich compounds, boron forms three-dimensional frameworks (e.g. boron icosahedra). Here, the metal is well protected by the surrounding boron polyhedrons, which are themselves very stable due to their strong bonding [1, 6]. It is also proposed, that the metal should have a stronger tendency to be oxidized, because the M-M and M-B bonds are longer and hence more easily broken than the B-B bonds [7].

In the following text, oxidation behavior at about 700 °C of some of the compounds, that are investigated in this work (TiB₂, AlB₂, CaB₆) will briefly be exemplified.

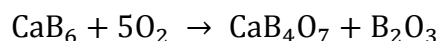
TiB₂ mainly forms crystalline TiO₂ (rutile) and crystalline or glassy B₂O₃ according to the reaction [37, 38]:



At temperatures around 700 °C, the oxidation rate is limited by diffusion through a dense oxide scale, following a parabolic law with a relatively low rate constant ($8 \times 10^{-5} \text{ g}^2 \text{ cm}^{-4} \text{ min}^{-1}$). Glassy B₂O₃ can melt and cover the surface at 450 °C, has a low oxygen diffusivity and hence can act as a protective layer [38]. Also the occurrence of TiBO₃ is reported, but may be considered as an intermediate step to the further oxidation resulting in TiO₂ and B₂O₃ [39].

AlB₂ as well shows a good oxidation resistance at temperatures up to 750 °C, which can also be attributed to liquid B₂O₃ limiting the oxidation rate. At earlier stages, the oxidation seems to be independent of oxygen partial pressure. It is reported, that B₂O₃ and Al₂O₃ rapidly react to form 2Al₂O₃ · B₂O₃ (Al₄B₂O₉), removing liquid B₂O₃ and increasing oxidation kinetics [40]. Native oxidation in air at room temperature exhibits a much higher oxidized fraction of aluminum than of boron [6].

CaB₆ forms predominantly ternary borates (CaB₄O₇, CaB₂O₄) and B₂O₃. In a temperature range of 400-700 °C the reaction



is supposed. The surface film of calcium borate acts as a protective layer, resulting in very good oxidation resistivity. In the temperature range of interest, nearly no weight gain was observed even for long exposures up to 25 hours [41, 42].

To the author's knowledge, no oxidation studies on AlYB₁₄ and ZrYB₁₄ are present in literature.

2.3 Bonding of metal borides

The available literature on binding energies of metal borides is rather meager. The most prominent source for binding energy reference values is the NIST (National Institute for Standards and Technology) XPS database [43]. This database holds only one reference from *Mavel et al.* [6] for each of overall four metal borides used in this work (AlB₂, TiB₂, VB₂, ZrB₂). *Mavel et al.* are the only ones who performed a comparative XPS study including a wide range of metal borides (19 binary and ternary metal borides) in 1973. Most other reference values can be found in publications that are not primarily focused on XPS. Literature values partially exhibit large scattering up to standard deviations of 2.72 eV and do often not include a charge control reference. To compare literature to measurements carried out in this work, binding energies of metal borides will be discussed in detail in the first part of results and discussion (see **Table 1**).

3. Methods

3.1 Sample preparation

Powders of TiB_2 (99.5% metal base purity), ZrB_2 (99.5% metal base purity excluding Hf), MgB_2 (99% metal base purity), CaB_6 (99% metal base purity) from *Alfa Aesar*, VB_2 from *Plansee* and a sintered piece of AlB_2 (offcut from a sputter target) from *Sindelhauser* were purchased. AlYB_{14} and ZrYB_{14} films and corresponding data (XRD, EDX) were provided by Oliver Hunold. ZrYB_{14} films were deposited during this work. TiB_2 films and corresponding data (XRD, EDX) were provided by Friederike Wittmers.

3.1.1 High power pulsed magnetron sputtering (HPPMS)

High power pulsed magnetron sputtering is a physical vapor deposition technique, in which power is applied to a sputter target in low duty cycles with a low frequency, leading to high peak power densities. This enables very dense, highly ionized plasma. The technique allows to deposit dense and smooth coatings, even on complex substrates [44]. AlYB_{14} and ZrYB_{14} films were synthesized in high vacuum systems with base pressures of 3×10^{-5} and 5×10^{-6} Pa at Ar (99.9999% purity) pressures of 0.9 and 0.6 Pa, duty cycles of 3.3% and 5% and temperatures of 25 and 750 °C, respectively.

3.1.2 Sintering

Sintering is a heat treatment with the goal of consolidating powder to one stable sample by grain growth and pore shrinkage, as illustrated in **Figure 2**. Evaporation and recondensation at the contact points fuses powder particles. Grain boundary diffusion followed by bulk diffusion drives the grain growth and pore shrinkage, leading to shrinkage, densification and hardening of the sintered body. The driving forces to trigger this mechanisms are reduction of surface energy, grain boundary energy, chemical potential gradients and mechanical stress [45]. Powders were grounded in a mortar

biased diode that absorbs photons, leading to the formation of electron-hole-pairs. Electrical pulses are created, whose intensity is proportional to the photon energy and allow for obtaining an energy dispersive X-ray spectrum [47]. EDX was carried out with an EDAX Genesis 2000 analyzer. Acceleration voltages were 6 kV for AlYB_{14} and ZrYB_{14} and 9 kV for TiB_2 films. An elastic recoil detection analysis (ERDA) measurement was used as a standard for the AlYB_{14} film.

3.2.3 X-ray diffraction (XRD)

X-ray diffraction is a popular, non-destructive method for structural analysis, enabling various applications as e.g. the determination of crystal symmetry and texture [48] or investigations on

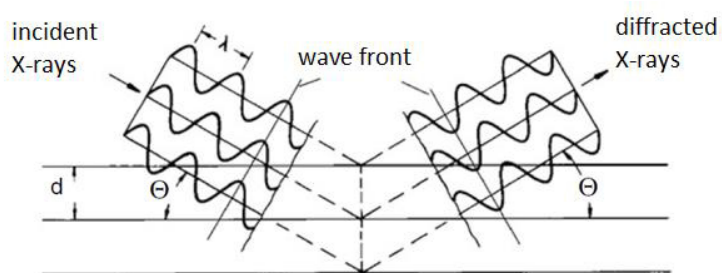


Figure 3: X-ray diffraction on crystal lattice planes [49]

phase diagrams [49] or stress [50]. A planar poly-crystalline sample is irradiated by X-rays and a detector moves around the sample, covering a range from ca. 0° to 120° , to electronically record the intensity of diffracted X-rays. Plotting intensities against the angle provides a diffractogram with peaks, which result from the X-rays diffraction on lattice planes, following Bragg's law: $n \cdot \lambda = 2d \sin(\theta)$, where θ is the diffraction angle, d is the interplanar spacing of lattice planes, λ is the wavelength of the X-rays and n is an integer, as shown in **Figure 3**. Powder diffraction was carried out in a Siemens D-5000 system with $\text{Cu-K}\alpha$ -radiation and Bragg-Brentano geometry, covering a 2θ range from 20° to 80° . All other diffraction was carried out in a Bruker AXS D8 Discover General Area Detection Diffraction System (GADDS) with $\text{Cu-K}\alpha$ -radiation and a grating incident angle of 15° , covering a 2θ range from 15° to 75° .

3.2.4 X-ray photoelectron spectroscopy (XPS)

X-ray photoelectron spectroscopy (XPS) is a non-destructive method for surface analysis, which provides information about the composition and chemical state of a sample. Incident X-ray photons with a given energy $E = h\nu$ cause photoemissions of electrons with kinetic energies E_k . Here h is Planck's constant and ν the frequency of the photon. According to $E_b = h\nu - E_k - \phi$, with ϕ as the work function (depending on the spectrometer), the binding energy E_b of an

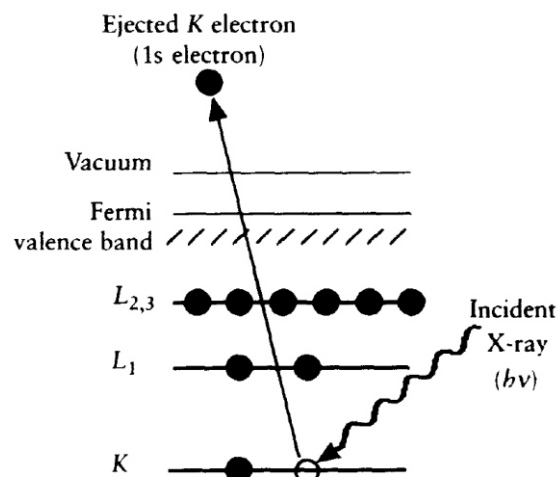


Figure 4: Photoemission of a core shell electron induced by incident X-rays [8]

electron can be calculated. Plotting E_b against the intensity results in a spectrum which is unique for every element in a compound, therefore allows for identifying single elements in a specific chemical state [8]. XPS was carried out in a JAMP-9500F system (JEOL) with an AlK α X-ray source (1486.5 eV) and a hemispherical electron energy analyzer in Fixed-Analyzer-Transmission-Mode with a pass energy of 20 eV. The electron take-off angle was perpendicular to the analyzer. The energy resolution was 0.1 eV. Energy calibration was carried out against the Au 4f 7/5 line (84.0 eV) and monitored several times during this work. Continuous irradiation can cause a charge up in poorly conductive samples. Possible charging of the sample was corrected according to the C 1s peak of adventitious carbon set to 284.8 eV, which is a commonly used value [51]. To assure a proper charge referencing, all regions of interest were scanned together with the C 1s peak and the high resolution spectra were adjusted accordingly. Depth profiling was carried out by Ar⁺ ion etching with an acceleration voltage of 2 keV. The etch rate was calibrated to be 9.1 nm/min for a SiO₂ standard. Even though sample rotation while etching can diminish angle dependent increase in surface roughness [8], it was not used here, because it favored redeposition of sputtered species in the

etching crater. Careful analysis of the acquired data is a crucial and highly labor-intensive part of gaining reliable information from XPS. In this work, analysis was conducted with the CasaXPS software. Standard Shirley backgrounds were applied to subtract noise from signal. For peak fitting and deconvolution of convoluted peaks, synthetic peaks with mixed Gaussian-Lorentzian line shapes (if not stated otherwise, 70% Gaussian – 30% Lorentzian) were employed. To consider the probabilities of certain subshell photoionizations in quantification, the raw peak areas were divided by the corresponding photoelectric cross sections, as calculated by *Scofield* [52]. Detailed information about the fitting of peak models is given in **Appendix 1**.

4. Results and discussion

In this work AlB_2 , CaB_6 , MgB_2 , TiB_2 , VB_2 , YB_6 , ZrB_2 , AlYB_{14} and ZrYB_{14} compounds have been investigated with XPS to determine binding energies and provide a comparison with literature values, which are presented in the first part of the following text. The second part will cover the main goal of this work, a depth profiling study of the oxide layers present on AlB_2 , TiB_2 , CaB_6 , AlYB_{14} and ZrYB_{14} .

Bonding

It is well known, that chemical impurities or phase impurities can cause changes in a compound's binding energies [8], therefore all samples, powders of CaB_6 , MgB_2 , TiB_2 , VB_2 , YB_6 and ZrB_2 , sintered samples of AlB_2 , CaB_6 , TiB_2 , VB_2 and ZrB_2 and thin films of TiB_2 , AlYB_{14} and ZrYB_{14} , have been analyzed regarding structure and chemical composition.

Chemical composition of thin films was determined by EDX. The actual stoichiometries were found to be $\text{Al}_{0.76}\text{Y}_{0.98}\text{B}_{14}$, $\text{Zr}_{0.45}\text{Y}_{0.47}\text{B}_{14}$ and $\text{Ti}_{0.5}\text{B}_2$. In $\text{Zr}_{0.45}\text{Y}_{0.47}\text{B}_{14}$ and $\text{Ti}_{0.5}\text{B}_2$, oxygen (0.6 at% and 8.6 at% respectively) and carbon (2.7 at% and 5.2 at% respectively) and in $\text{Al}_{0.76}\text{Y}_{0.98}\text{B}_{14}$, oxygen (2.5 at%) were detected. In $\text{Zr}_{0.45}\text{Y}_{0.47}\text{B}_{14}$ and $\text{Ti}_{0.5}\text{B}_2$, F (0.2 at%) and Al (8.3 at%) were detected, respectively. Composition of powders and sintered samples was probed by XPS. The XPS analyzer also picked up minor signals from the steel sample holder, containing Fe, Cr, Co, Mn, Al, Ca and probably Mg (in survey scans, the Mg 2p peak partially overlaps with Fe and Co 3s peaks due to insufficient

resolution). Hence, an evidence for the presence of these elements in the sample cannot be clearly given. In most sintered samples, Mg contributions decreased with ion etching time. This can be attributed to evaporation and condensation of Mg from MgB_2 in the sintering chamber. Traces of Si in TiB_2 and ZrB_2 powders and N in VB_2 powder were detected but also decreased with proceeding ion etching and hence are ascribed to surface contamination, which may originate from manufacturing of the powders. The B/M ratios were generally higher than those of ideal stoichiometries. This might be partly caused by boron rich surface contamination that still remained on rough samples after maximum ion etching time and by the relatively high kinetic energy of B 1s electrons compared to Ti 2p and V 2p electrons leading to a larger escape depth of B 1s electrons. However, a slight boron abundance seems to be generally present and can also be observed in the samples probed by EDX. An exception is CaB_6 , where the B/Ca ratios are 3.9 and 4 for powder and sintered samples, respectively. This may indicate the presence of CaB_4O_7 , which will be discussed later in detail.

Structure of all samples was analyzed by XRD. $\text{Al}_{0.76}\text{Y}_{0.98}\text{B}_{14}$ and $\text{Zr}_{0.45}\text{Y}_{0.47}\text{B}_{14}$ films are X-ray amorphous. It was shown with XPS by *Music et al.* [53] that amorphous AlYB_{14} films exhibit icosahedral boron bonding like the crystalline counterpart. Since the B 1s binding energies of $\text{Al}_{0.76}\text{Y}_{0.98}\text{B}_{14}$ and $\text{Zr}_{0.45}\text{Y}_{0.47}\text{B}_{14}$ are identical (187.8 eV) the same can be assumed for amorphous ZrYB_{14} films. The $\text{Ti}_{0.5}\text{B}_2$ film exhibits only peaks belonging to TiB_2 . Diffractograms of CaB_6 , VB_2 , ZrB_2 , TiB_2 , YB_6 , MgB_2 and AlB_2 are shown in **Figure 5 a)-g)**. Diffractograms of CaB_6 , VB_2 , ZrB_2 and TiB_2 powders and sintered samples are displayed together for comparison. In all samples, the expected main phase was detected. CaB_6 (**Figure 5 a)** powder exhibits small peaks that can be attributed to different calcium borates like $\text{Ca}_3(\text{BO}_3)_2$, $\text{Ca}_2\text{B}_2\text{O}_5$ and predominantly CaB_4O_7 . These peaks become more pronounced after sintering. The fact that these compounds are clearly visible at an incident angle of 15° , suggests that they are not only present as a minor surface contamination, but are incorporated in the pristine boride. Probably crystalline areas of these compounds agglomerated from surface oxides and borates of the powder during sintering. VB_2 (**Figure 5 b)** powder contains visible amounts V_2B_3 and VB , though the latter is partially overlapping with VB_2 . After sintering these amounts increase. ZrB_2 (**Figure 5 c)** powder is mostly phase pure, hardly visible contributions of ZrB_{51} seem to

be present. After sintering, these contributions become more obvious. TiB_2 (**Figure 5 d**) powder is phase pure. After sintering, TiB contributions appear. YB_6 (**Figure 5 e**) powder contains a variety of different phases beside YB_6 , mostly YB_4 but also YB_2 , YB_{12} , YB_{66} and β -rhombohedral boron. MgB_2 (**Figure 5 f**) powder exhibits contributions of MgB_4 and MgO . Sintered AlB_2 (**Figure 5 g**) contains large amounts of AlB_{12} . For most of the compounds mentioned above, sintering at very low pressures in the range of 10^{-6} Torr apparently resulted in the formation or increase of phases different from the main phase. The following discussion shows that this has an effect on measured binding energies.

Table 1 contains the measured binding energies of several transitions for all samples used in this work and corresponding mean reference values compiled from literature. Whenever the adventitious C 1s peak was used as a charge control reference in literature, the binding energy values were corrected to a C 1s value of 284.8 eV. However, a charge control reference was not given in many of the used references. A charge-up was observed in some compounds in this work, hence literature values without charge referencing might be less reliable. Measured binding energies, presented in **Table 1**, are discussed in the following text. Out of 27 comparable measured values, 14 are in good agreement with literature. Some of the deviating values differ up to 3.5 eV from references. Also, for some compounds, there are quite large differences between the powder and sintered sample up to 1.0 eV.

The AlB_2 Al 2p values is slightly higher than the mean literature value, which may be explained by the presence of AlB_{12} , for which a higher binding energy was reported [6]. In contrast, the B 1s value is 1.4 eV lower than the only reported value by *Mavel et al.* [6], which might be due to the author's apparently low energy resolution and resulting vague deconvolution of boride and oxide peaks.

The CaB_6 2p $3/2$ value of the powder is about 0.1 eV above literature values while the sintered sample exhibits a lower value. Another component at lower binding energy that was assigned to CaB_6 appeared in the Ca 2p spectra of the sintered sample with proceeding ion etching.

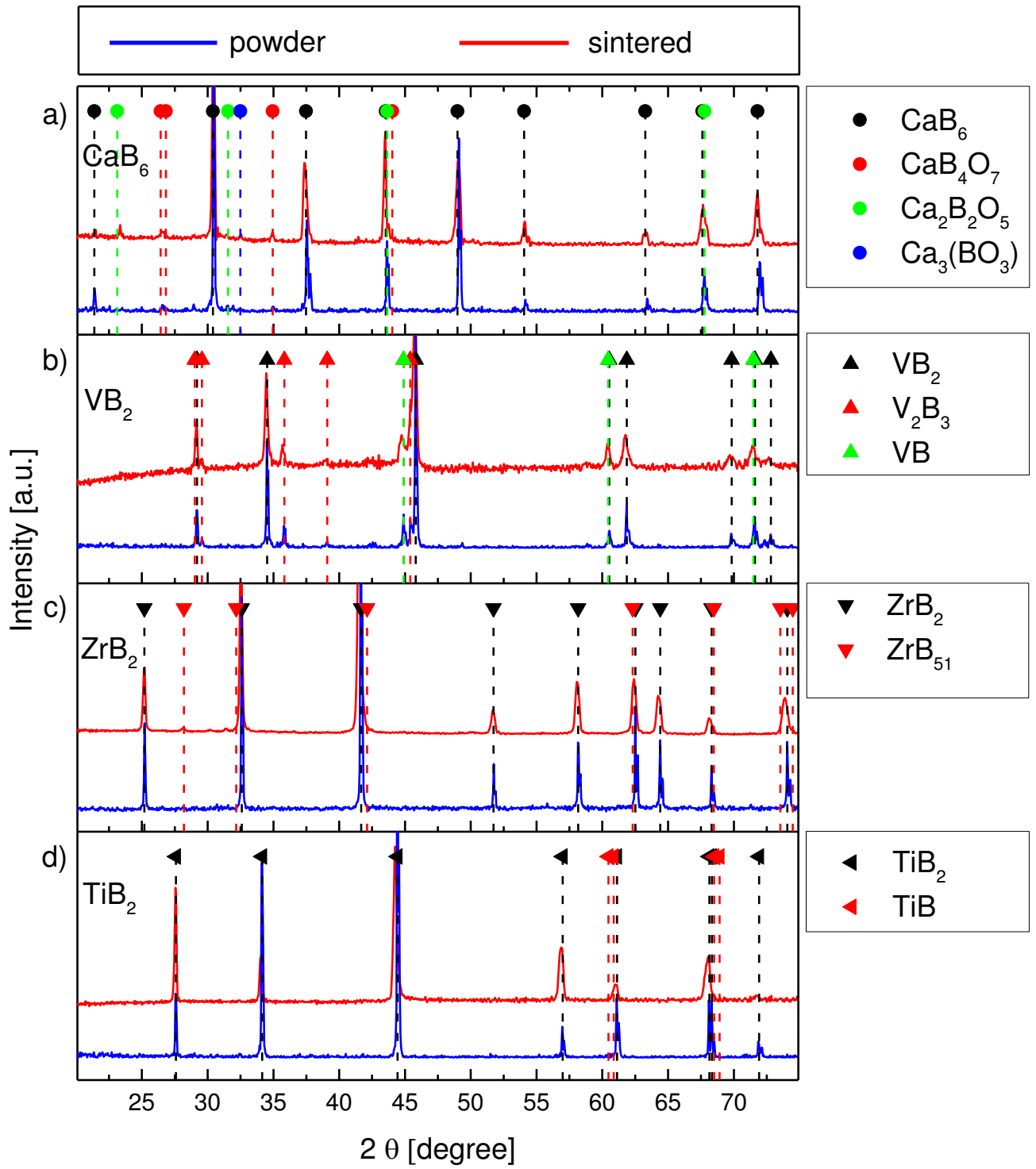


Figure 5: Diffractograms of powder and sintered a) CaB_6 , b) VB_2 , c) ZrB_2 and d) TiB_2

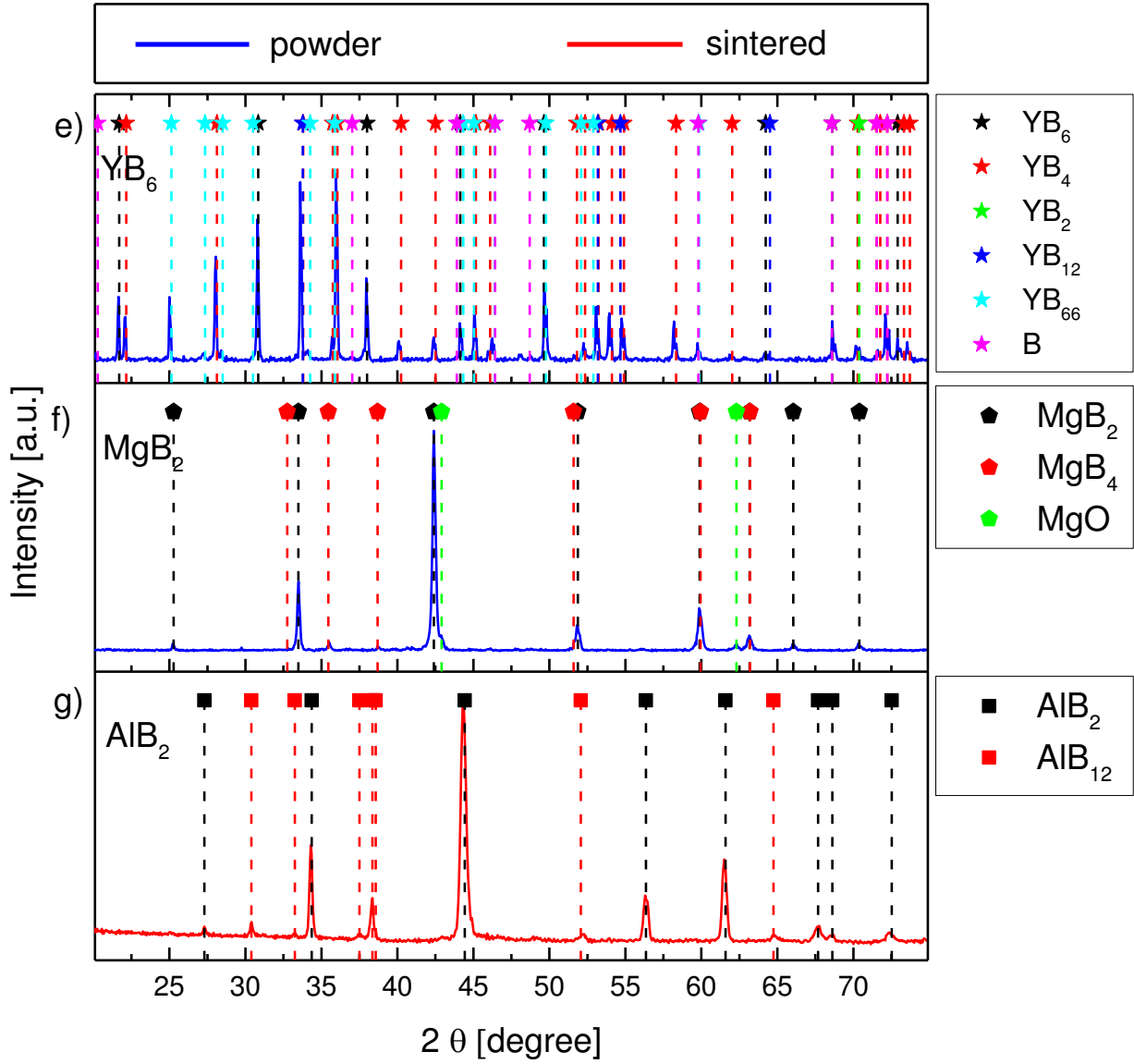


Figure 5 (continued): Diffractograms of e) powder YB_6 , f) powder MgB_2 and g) sintered AlB_2

Hence, the prior component at higher binding energy, which was also found in the powder spectra, can be assigned to some form of calcium borate. The presence of calcium borates was proved by XRD and it is likely that *Shi et al.* [54] and *Zhang et al.* [55], who cited *Shi et al.* [54], spuriously measured calcium borate instead of CaB_6 . Their reported B1s values, both 192.6 eV, are much higher than usually seen in metal borides (up to 188.2 eV measured in this work) and are more suitable for B_2O_3 [56], hence indicate a bonding with oxygen. CaO can be excluded, since its Ca 2p 3/2 value (346.6 (± 0.5) eV [43]) is lower. The major increase of the B 1s value of 1 eV from powder to sintered sample probably originates from the presence of calcium borates in the sample's bulk. The

measured B 1s peak might actually be the summation of overlapping contributions of calcium borate and CaB_6 , hence the powder value seems more reliable.

While the MgB_2 B 1s value is within the range of literature, the Mg 2p value is about 1.6 eV lower than the mean literature value. Since there are many reference values and their standard deviation is not large enough to include the measured value, the present amount of MgB_4 might be crucial. Also the measured 2p peak deconvolution might not be distinct. Only MgO and MgB_2 were considered. For magnesium borates, no binding energy reference values could be found.

TiB_2 powder and film exhibit nearly identical binding energy values, which are in good agreement with literature. The Ti 2p $3/2$ and $1/2$ values of 454.1 and 460.0 eV, respectively, are in perfect agreement with those reported by *Rivière et al.* [57], who did a charge referencing to adventitious carbon. The sintered sample values are about 0.3 eV higher, which probably originates from the presence of TiB in the sintered sample.

VB_2 V 2p values differ about 0.3 eV from powder to sintered sample and are below the range of literature values. Since literature values are in good agreement with each other, the lower measured values probably originate from the presence of V_2B_3 and VB in the samples.

Values measured for YB_6 are probably not reliable because of the extensive amount of phase impurities in the powder. A distinct identification of the bonding ascribed to YB_6 via XPS based on these values is hence not possible. Since YB_6 and AlYB_{14} XRD peaks are overlapping, an identification of their particular bonding via XPS would be useful for determining present species in Al-Y-B thin films [58] without resorting to elaborate techniques like transmission electron microscopy.

The binding energies of ZrB_2 do not differ significantly before and after sintering and are in good agreement with literature, except the B 1s value after sintering, which is about 0.5 eV higher than that of the powder. The increased amount of ZrB_{51} in the sintered sample seems to have a strong influence on the bonding of boron. In contrast to two dimensional boron sheets in ZrB_2 , boron rich phases are known to form complex three dimensional boron frameworks, hence it is likely that the measured binding energy of boron changes while the metal is less affected.

It is shown that the measured metal diborides B 1s values spread on a range from 187.0 to 188.2 eV. In $\text{Al}_{0.76}\text{Y}_{0.98}\text{B}_{14}$ and $\text{Zr}_{0.45}\text{Y}_{0.47}\text{B}_{14}$ films the B 1s (187.8 eV) and Y 3d (156.5 and 158.5 eV for 5/2 and 3/2, respectively) values are identical, suggesting that the systems' binding energies are dictated by the icosahedral boron framework and that the metal species have no major influence. In contrast, different metal species lead to a B 1s range of 1.2 eV in diborides.

These results show that phase impurities can have a strong influence on measured binding energies and that it is important to use both chemical and phase pure samples to obtain precise values. Such impurities might also have been a reason for the scattering in literature values. Another probable reason is the absence of a proper charge control in many publications. A charge control reference was used by 67% of authors cited for the B 1s value of TiB_2 , while only 22% of authors cited for the B 1s value of MgB_2 did so. The standard deviations are 0.1 and 0.8, respectively.

Depth profiles of oxide layers

TiB_2 , AlYB_{14} and ZrYB_{14} thin films and AlB_2 and CaB_6 sintered samples were oxidized at 700 °C in air for 5 minutes. XPS depth profiling was performed in order to determine the buildup of oxide layers on metal borides with different boron content. High resolution XPS spectra were deconvoluted for quantification of the components. The change in these spectra of TiB_2 , AlB_2 , CaB_6 and ZrYB_{14} as a function of ion etching time is shown in **Figure 6**. AlYB_{14} is left out in the figure because B 1s and Y 3d spectra are very similar to those of ZrYB_{14} and the Al 2s spectrum exhibits a very low intensity. The component contents are presented as a function of etch time and not of the actual depth. The sputter rate differs between different compounds and precisely determining it would require standards of every sputtered species. Furthermore, there are aspects that would distort the measured values, if they were presented as a function of depth: it was observed that the ion gun used in this work scanned a larger area than it should, which could have led to redeposition of sputtered species in the etching crater. The analyzer's focusing lenses did not only collect signals from the main etching crater. Different bond strengths could result in preferential sputtering of some

Table 1: Measured binding energies of all samples and corresponding literature values

Compound	Transition	Sample Type	Measured Binding Energy [eV]	Compiled Literature Value (\pm Std. Dev.) [eV]	Number of Reference Values	References
AlB₂	Al 2s	sintered	117.1	not available		
	Al 2p	sintered	72.0	71.5 (± 0.4)	2	[6, 59]
	B 1s	sintered	187.1	188.5	1	[6]
CaB₆	Ca 2p 3/2	powder	348.3 *	348.1 (± 0.1)	2	[54, 55]
		sintered	346.6			
	Ca 2p 1/2	powder	351.8 *	not available		
		sintered	350.3			
	B 1s	powder	187.2	190.7 (± 2.7)	3	[27, 54, 55]
		sintered	188.2			
MgB₂	Mg 2p	powder	47.3	49.9 (± 0.6)	9	[60-67]
	B 1s	powder	187.0	187.2 (± 0.8)	9	[60-67]
TiB₂	Ti 2p 3/2	powder	454.1	454.5 (± 0.3)	4	[6, 57, 68, 69]
		sintered	454.5			
		film	454.2			
	Ti 2p 1/2	powder	460.0	460.3 (± 0.3)	2	[57, 69]
		sintered	460.3			
		film	460.0			
	B 1s	powder	187.5	187.5 (± 0.1)	6	[6, 57, 68-71]
		sintered	187.8			
		film	187.5			

* the binding energy value probably belongs to a calcium borate and not to CaB₆

Table 1 (continued): Measured binding energies of all samples and corresponding literature values

Compound	Transition	Sample Type	Measured Binding Energy [eV]	Compiled Literature Value (\pm Std. Dev.) [eV]	Number of Reference Values	References
VB₂	V 2p 3/2	powder	512.5	513.5 (± 0.2)	3	[6, 72, 73]
		sintered	512.8			
	V 2p 1/2	powder	520.1	not available		
		sintered	520.4			
YB₆	B 1s	powder	187.3	188.1 (± 0.2)	3	[6, 72, 73]
		sintered	188.0			
	Y 3d 5/2	Powder	157.2	not available		
	Y 3d 3/2	powder	159.4	not available		
ZrB₂	B 1s	powder	187.6	not available		
		powder	179.2	not available		
	Zr 3d 5/2	sintered	179.3	179.0 (± 0.3)	8	[36, 74-80]
		powder	181.5	181.4 (± 0.3)	7	[74-80]
AlYB₁₄	Zr 3d 3/2	sintered	181.5	187.9 (± 0.4)	7	[36, 74, 75, 77-79, 81]
		powder	187.7			
	B 1s	Sintered	188.2	not available		
		film	118.6**			
ZrYB₁₄	Y 3d 5/2	film	156.5	not available		
	Y 3d 3/2	film	158.5	not available		
	B 1s	film	187.8	not available		
	Zr 3d 5/2	film	179.6	not available		
ZrYB₁₄	Zr 3d 3/2	film	182.0	not available		
	Y 3d 5/2	film	156.5	not available		
	Y 3d 3/2	film	158.5	not available		
	B 1s	film	187.8	not available		

** the binding energy value is relatively high and may not be accurate due to a poor deconvolution of the corresponding peak

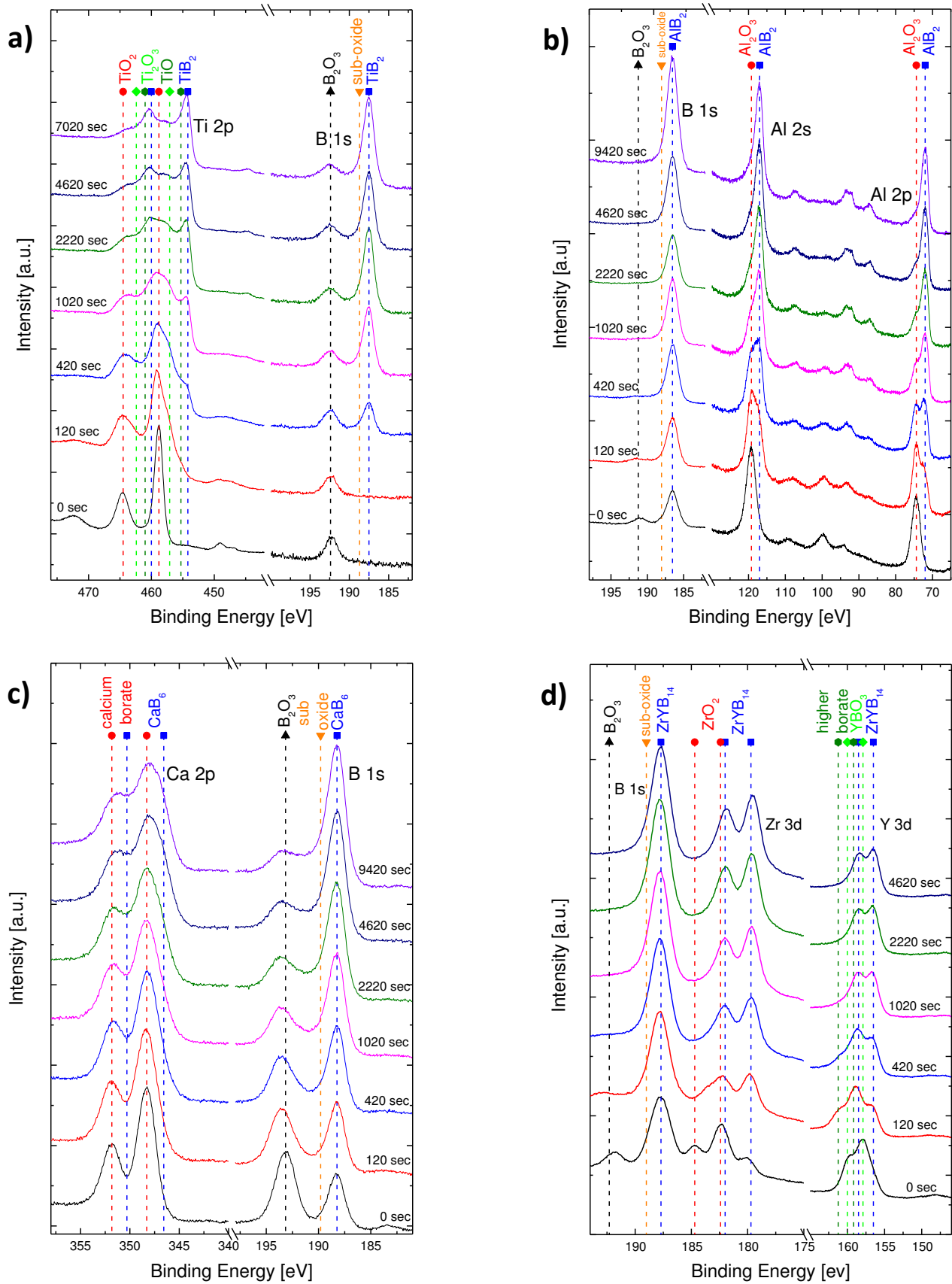


Figure 6: Change in the XPS spectra of a) TiB_2 , b) AlB_2 , c) CaB_6 and d) ZrYB_{14} as a function of ion etching time, peak intensities have been modified to emphasize shape changes and are not true

species. A rough sample surface could shadow regions from the ion beam, resulting in a signal pickup from differently etched regions. The surface roughness values of TiB_2 , AlB_2 , CaB_6 , ZrYB_{14} and AlYB_{14} were 0.056, 0.155, 1.292, 0.022 and 0.021 μm , respectively. Hereafter the results of the depth profiles are reported and discussed.

TiB₂: **Figure 7** shows the contents of Ti 2p and B 1s signals belonging to components of the oxide layer and the film beneath as a function of etch time. Only

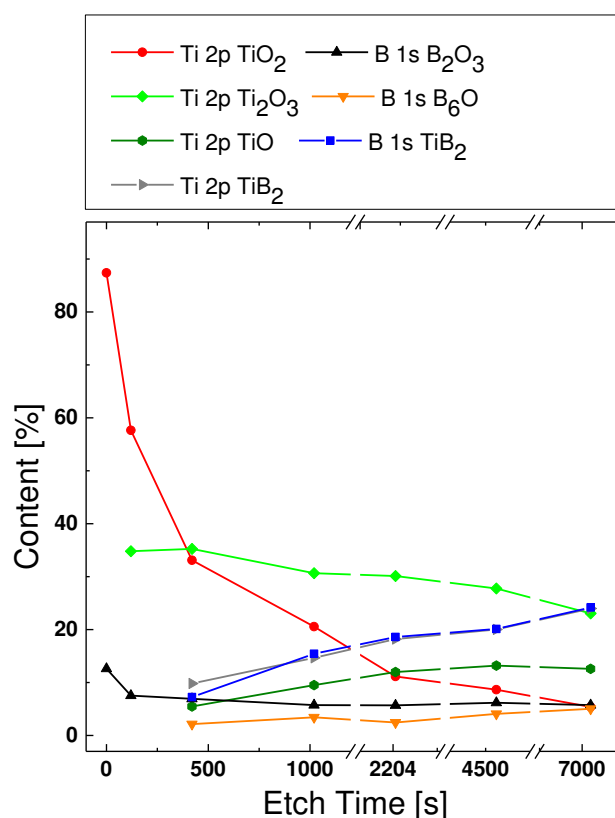


Figure 7: Depth profile determined from the XPS spectra peaks of TiB_2

TiO_2 and B_2O_3 are present at the surface, whereat TiO_2 is the predominant compound. TiO_2 content drops fast, revealing underlying oxides Ti_2O_3 and TiO . The former continuously decreases, while the latter does not decrease until the last measuring point. These trends suggest a distribution of titanium oxides with higher oxidized states at surface and lower oxidized states close to the film. However, the measured trends may not represent the original distribution of titanium oxides, as it is known that ion sputtering can cause their reduction. This especially refers to the probability of reduction from TiO_2 to Ti_2O_3 , which was reported to be ten times higher than that from Ti_2O_3 to TiO [82]. The B_2O_3 signal drops in the beginning, then settles to a constant value, suggesting that this oxide is predominantly present at the surface but to minor amounts also in the rest of the layer. B_6O is not present at the surface, but appears with a slightly increasing contribution closer to the film. It is shown that titanium is more oxidized than boron and that higher oxidized states are predominantly located at the surface. Ternary titanium borates were not identified. The change in TiB_2 XPS spectra as a function of etch time is shown in **Figure 6 a)**.

AlB₂: **Figure 8** shows the contents of Al 2s and B 1s signals belonging to identified components. B₂O₃ seems to be only present at the surface near region, while B₆O content is present in the whole layer. The initial increase in its signal suggests that it is predominantly located in the lower regions of the layer, while the later increase is probably due to its relatively strong resistivity to ion etching.

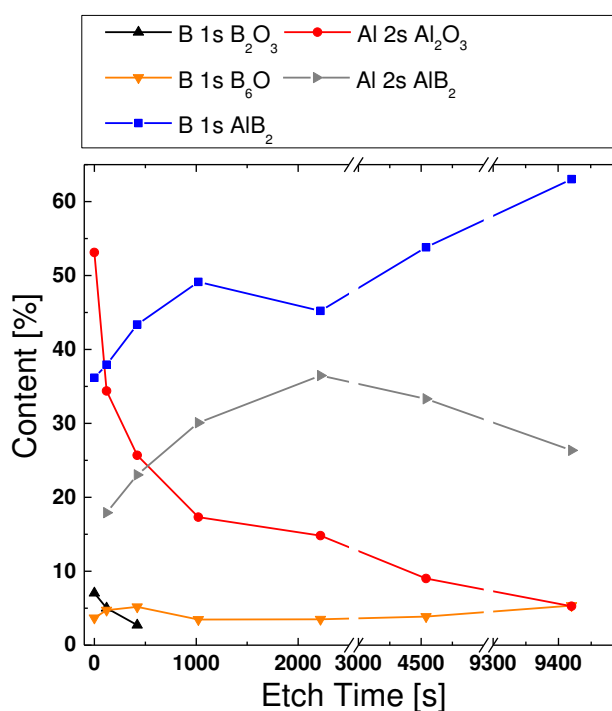


Figure 8: Depth profile determined from the XPS spectra peaks of AlB₂

B₆O exhibits an icosahedral boron framework, resulting in a strong bonding [56]. Al₂O₃ is the major component at the surface and decreases rapidly as a function of etching. The kink in the B 1s curve of AlB₂ probably results from the relatively high increase of Al 2s of AlB₂ and low decrease of Al 2s of Al₂O₃. The later decrease of Al 2s of AlB₂ can be ascribed to a boron abundance in the sample (the B/Al ratio is 2.12), resulting in a higher intensity of the B 1s signal, relative to the Al 2s signal. Aluminum borates were not detected. Similar to TiB₂, metal is much more oxidized than boron and higher oxides are predominantly present at the surface. The absence of B₂O₃ in the lower regions of the oxide layer might hint to the formation of a protective Al₂O₃ layer. The change in AlB₂ XPS spectra with proceeding etch time is shown in **Figure 6 b**).

CaB₆: **Figure 9** shows the contents of Ca 2p and B 1s signals belonging to identified components. The presence of calcium borates was proven by XRD and a B/Ca ratio of 4 suggests that CaB₄O₇ is the major present borate. Reliable binding energy reference values for calcium borates were not found. The O/(Ca+B) ratio of CaB₄O₇ is 1.4 and close to the O/B ratio of B₂O₃, which is 1.5. Since the amount of oxygen generally is an indicator for the extent of chemical shifts of binding energies, it is likely that a part of the B 1s signal of B₂O₃ actually originates from calcium borate. The

initial rapid drop in the B 1s signal of B_2O_3 can be attributed to the removal of B_2O_3 and probably also calcium borate, located at the surface. The Ca 2p signal of calcium borate also decreases fast in the beginning, while CaB_6 and B_6O signals rise rapidly. These trends suggest that, even though calcium borates are incorporated in the pristine boride, they are also a major component of the oxide layer. B_6O is rarely present at the surface and increases with proceeding depth, similar

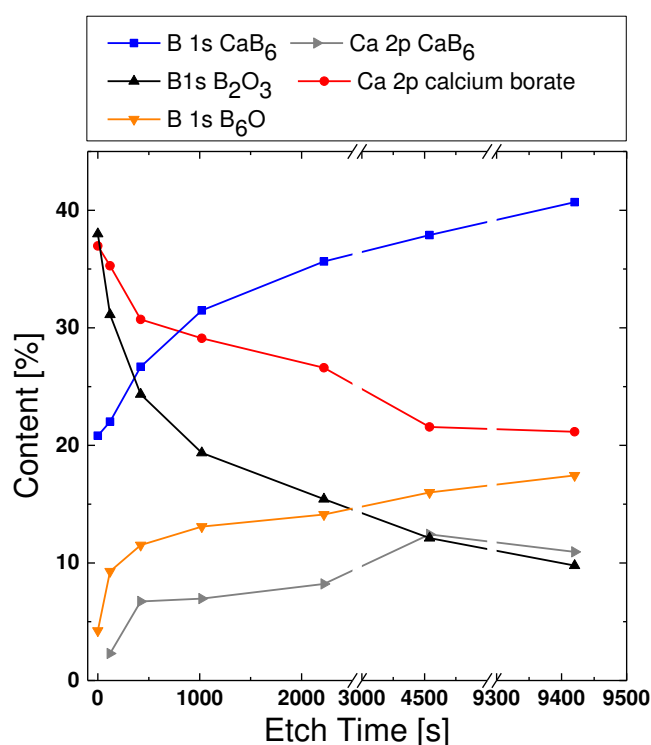


Figure 9: Depth profile determined from the XPS spectra peaks of CaB_6

as in TiB_2 and AlB_2 . It seems that calcium and boron exhibit a similar degree of oxidation, even though this is hard to clarify because the origin of the B 1s signal attributed to B_2O_3 is ambiguous. Also, the high surface roughness of the sample may distort the trends. CaO was not detected. The change in CaB_6 XPS spectra as a function of etch time is shown in **Figure 6 c**).

ZrYB₁₄: **Figure 10** shows the contents of Zr 3d, Y 3d and B 1s signals belonging to identified components. B_2O_3 and ZrO_2 are only present in the surface near regions. The B 1s signal of B_6O increases with proceeding depth, suggesting it is predominantly present in the layer's lower regions. At the surface, an additional component in the Zr 3d signal was observed, which was attributed to surface defects, namely oxygen vacancies in ZrO_2 . These are known to form by substitution of Zr^{4+} cations with Y^{3+} and were also predicted in nanocrystalline cubic ZrO_2 [83]. These defects were annealed by the first ion sputtering cycle. The Y 3d signal of YBO_3 rapidly drops after the first etching and then slowly decreases. YBO_3 might be relatively resistant to ion etching due to its strong octahedral boron framework [84]. The initial drop is also visible in the B 1s signal of $ZrYB_{14}$, which has an icosahedral boron framework. It is likely that the octahedral and icosahedral boron bonds exhibit similar binding energies and hence, that part of the B 1s signal ascribed to $ZrYB_{14}$ actually originates

from YBO_3 . Simultaneously to this drop, a component about 1.3 eV above YBO_3 increased. Since chemical shifts in this direction usually originate from incorporation of more oxygen, this component can be ascribed to a higher yttrium borate. This component vanishes quickly and was probably created by ion sputtering. The Y 3d binding energies of ZrYB_{14} and Y_2O_3 are too similar to be distinguished, but ZrO_2 can be used as a reference, since the energies of formation of

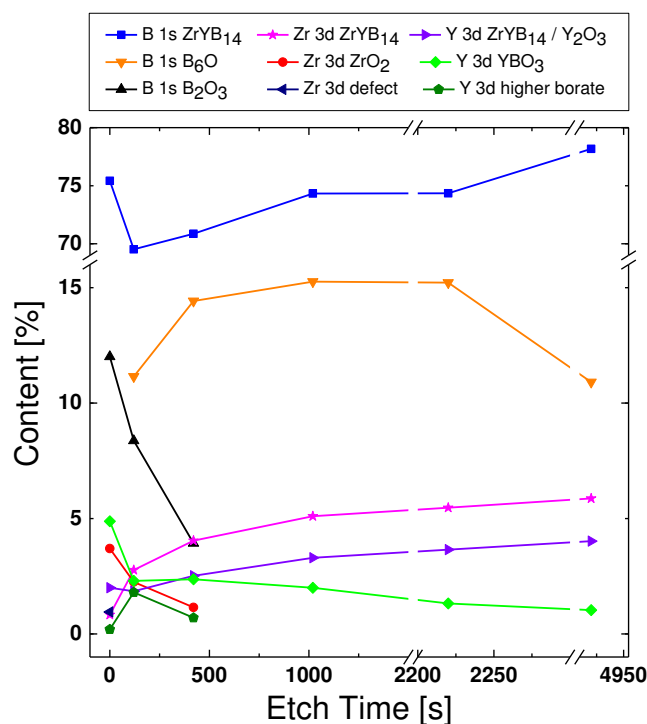


Figure 10: Depth profile determined from the XPS spectra peaks of ZrYB_{14}

ZrO_2 and Y_2O_3 (-36699 and -386911 J/mol, respectively [85]) are very similar. The Zr/Y peak area ratio of the Zr 3d signal of ZrYB_{14} and the Y 3d signal of $\text{ZrYB}_{14}/\text{Y}_2\text{O}_3$ is about 1.8 for every measurement except for the surface scan, where it is 0.5. This suggests that Y_2O_3 is only present at the surface. Taking the high boron content into account, boron is not heavily oxidized compared to the metals. Intense signals from ZrYB_{14} are visible from the surface measurement on, which shows that the overall oxide layer thickness has to be significantly thinner than that of the compounds discussed before. The change in ZrYB_{14} XPS spectra as a function of etch time is shown in **Figure 6 d**).

AlYB₁₄: **Figure 11** shows the contents of Al 2s, Y 3d and B 1s signals belonging to identified components. The observations for the B 1s and Y 3d signals are generally very similar to the ones in ZrYB_{14} . The initial drop of the Y 3d signal of YBO_3 is less significant than for ZrYB_{14} and no drop in the B 1s signal of AlYB_{14} was observed, so relatively less YBO_3 seems to be present. The Y 3d signal of $\text{AlYB}_{14}/\text{Y}_2\text{O}_3$ initially decreases, then increases, suggesting that Y_2O_3 is only present at the surface as for ZrYB_{14} . The deconvolution of the Al 2s peak is relatively imprecise due to its very low intensity. Reference values for binding energies of aluminum borates were generally too high to match and references for aluminum yttrium borates or yttrium aluminates could not be found. Since the Y 3d

peak was very similar to the one of ZrYB_{14} , it was assumed that no Y-Al-O, Y-Al-B or Y-Al-B-O phases were present and only Al_2O_3 and AlYB_{14} were considered as components contributing to the Al 2s peak. Al_2O_3 is predominantly present in surface near regions. As for ZrYB_{14} , initially intense signals from AlYB_{14} indicate an overall thin oxide layer.

The results presented above show that the investigated metal diborides generally oxidize more than the boron rich ZrYB_{14} and AlYB_{14} films. This may

be attributed to compound structure, as suggested by *Mavel et al.* [6]. The strongly bonded icosahedral boron framework in these boron rich compounds makes both boron and metal hardly accessible. For the diborides, the metal is oxidized more than boron. This was also observed on natively oxidized TiB_2 , ZrB_2 , and MgB_2 . Regarding the quantitative availability of boron and metals in ZrYB_{14} and AlYB_{14} , the oxidation of boron is relatively low. This might be ascribed to the relatively high strength of B-B bonds, compared to M-B and M-M bonds, as supposed by *Odintsov et al.* [7]. Within this comparison it is difficult to include CaB_6 because of its incorporation of borates in the pristine boride. Higher oxides are rather located in surface near regions while sub-oxides are located in the lower parts of the oxide layer. B_2O_3 and B_6O are present in all samples. Some ternary metal borates were identified. Since more possible ternary borates and oxides are known, this shows the necessity of reliable references for binding energy values to certainly identify all observed components.

The data presented so far provide information of the relative quantities of different oxides and borates. To draw a more transparent comparison of the overall degrees of oxidation, it can be

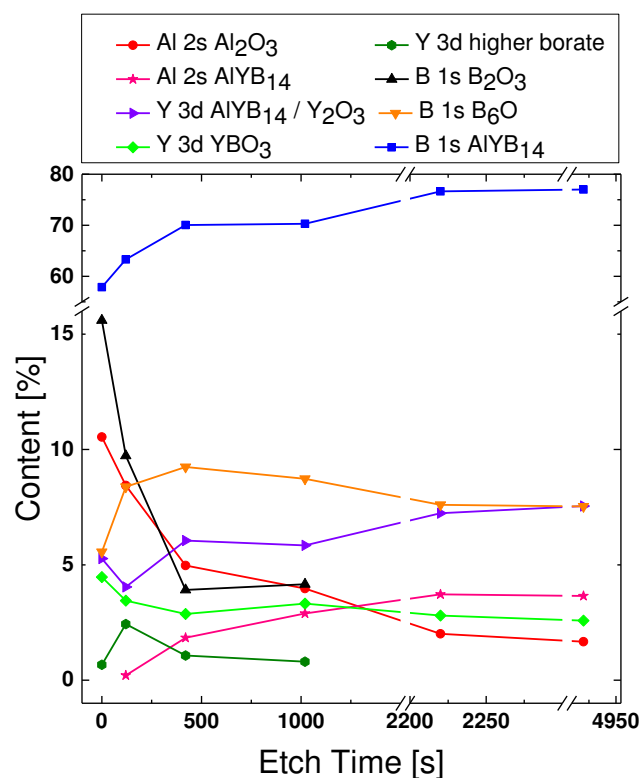


Figure 11: Depth profile determined from the XPS spectra peaks of

adjuvant to know the thickness of the oxide layers. Obtaining precise values for the overall oxide layer thickness on the samples by measurements (scanning electron microscopy, XPS line scans) was not possible because the layers were too thin. However, there is a model for estimating oxide layer thicknesses by XPS that has been used by *Mathieu et al.* in several publications [86-88]. The layer thickness is estimated by comparing the intensities of the oxidized and non-oxidized component signals. A detailed explanation of the model is given in **Appendix 2**. *Mathieu et al.* assumed a uniform step-like concentration profile of a single oxide species on a metal substrate. To transfer this assumption, calculations were carried out as if only one type of oxide/borate was covering the sample. Every elemental signal from the underlying metal boride was compared to the oxide/borate in which it was mostly present. Minor or unidentified components were not considered. The oxides and borates can be distributed quite differently in the overall oxide layer, homogeneously mixed or structured in layers [89], therefore a possible range for the overall layer thickness can be reached ranging from the highest value for a single type of oxide/borate to the sum of all present types. The results of these calculations give a semi-quantitative evaluation of the overall degree of oxidation of the investigated samples and are presented in **Figure 12**. The values calculated for CaB_6 are not very meaningful for the overlayer thickness because of the incorporation of calcium borates in the pristine boride and the B_2O_3 signal probably partially originates from calcium borates. **Figure 12** confirms the previous observation that ZrYB_{14} and AlYB_{14} oxidize less than the diborides. For AlB_2 the metal oxide is much thicker than the boron oxide, as it was suggested by the previous results. In contrast, this is not observed for TiB_2 , probably because Ti_2O_3 and TiO , which were also present to a noteworthy extent, were not considered. ZrYB_{14} and AlYB_{14} also exhibit a thin B_2O_3 and YBO_3 thickness, representing a low degree of boron oxidation. These calculations confirm the assumptions discussed in the previous paragraph and provide a way to quantitatively compare the overall degree of oxidation.

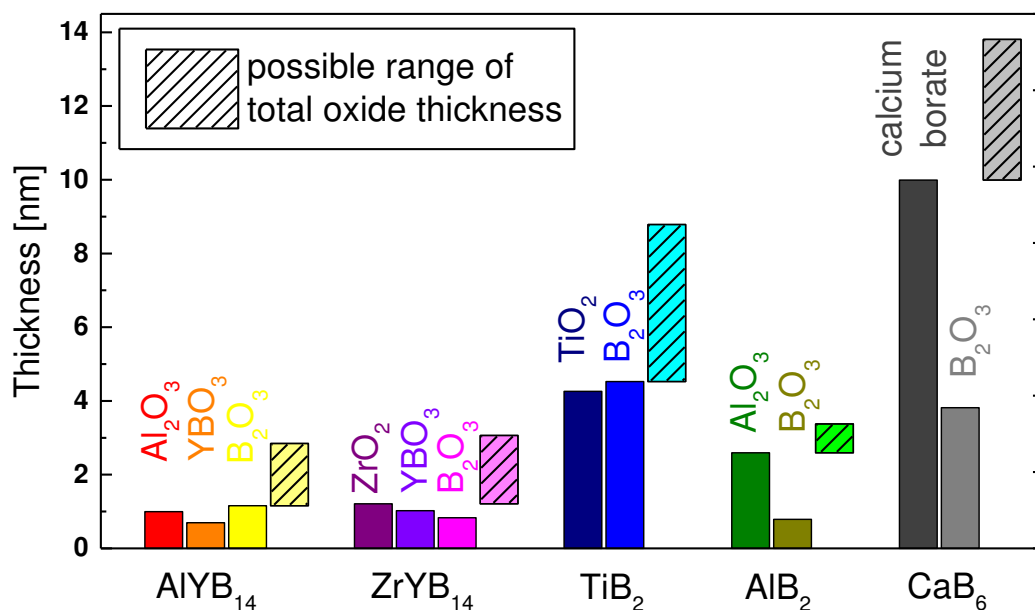


Figure 12: Calculated oxide/borate layer thickness of AlYB₁₄, ZrYB₁₄, TiB₂, AlB₂ and CaB₆

5. Conclusion

Binding energies of AlB₂, CaB₆, MgB₂, TiB₂, VB₂, YB₆, ZrB₂, AlYB₁₄ and ZrYB₁₄ were measured with XPS. Good agreements with literature values were observed for ZrB₂ and TiB₂, which were mostly phase pure. Deviations from literature were predominantly observed for samples with higher phase impurities like MgB₂, AlB₂ and VB₂. These impurities might be the reason for deviation from some literature values. Partially high scattering of literature values might be attributed to missing charge control in some publications. Sintering at low pressure had an effect on the samples structural composition. Comparison of powder and sintered samples by XRD revealed an increase in phase impurities that came along with significant changes in binding energies, especially for TiB₂, VB₂ and the B 1s value of ZrB₂. These changes emphasize the influence of phase impurities on measured binding energies. Measured B 1s binding energies of metal diborides spread within a range of 1.2 eV, while AlYB₁₄ and ZrYB₁₄ exhibit identical values for each B 1s and Y 3d binding energies. This suggests that, with increasing boron content, the electronic structure is predominantly dictated by the boron framework. Due to the extensive amount of phase impurities in YB₆, the measured binding energy values cannot reliably be used as references for the identification of the bonding in this phase.

The oxygen induced change in binding energies was used to identify compounds in oxide layers present on the oxidized samples of TiB_2 , AlB_2 , CaB_6 , ZrYB_{14} and AlYB_{14} . XPS depth profiling with Ar^+ ion etching was carried out to obtain the corresponding depth profiles of the layers. Thin film samples exhibited a lower surface roughness than sintered samples, which makes them more suitable for ion etching. B_2O_3 and B_6O seemed to be components of all investigated oxide layers. Higher oxidized states were generally observed in surface near regions, while lower oxidized states were predominantly located close to the oxide-boride interface. Possible oxide layer thickness was calculated to obtain a semi-quantitative evaluation of the degree of overall oxidation. It was shown that AlYB_{14} and ZrYB_{14} oxidized less than TiB_2 and AlB_2 , which may be attributed to the strongly bonded icosahedral boron framework of AlYB_{14} and ZrYB_{14} that limits the accessibility of both boron and metals. In TiB_2 , AlB_2 , CaB_6 , AlYB_{14} and ZrYB_{14} , boron is relatively less oxidized than metal. This may be ascribed to the higher strength of B-B bonds compared to M-B and M-M bonds. CaB_6 could not be unambiguously included in this comparison due to the incorporation of calcium borates in the pristine boride.

6. Future work

To improve the quality of binding energy data, substances of high chemical and phase purity are required. Reliable values might enable the identification of different bonding for example in Al-Y-B and other ternary metal boride thin films. A systematic study on the dependence of the bonding on boron content would generally be interesting in a metal boride system like Y-B with a wide range of possible phases (YB_2 , YB_4 , YB_6 , YB_{12} , YB_{66}). Regarding the commercial powders and sintered samples in this work, it seems to be challenging to synthesize bulk metal borides with high phase purity, whereas the TiB_2 thin film is phase pure. Therefore, thin films deposited from elemental targets should be considered for further measurements. Since the identification of components in the oxide layers was not always unambiguous, it would also be desirable to provide reference values for more complex oxides and borates.

To solidify the assumption that boron rich compounds generally inhibit a better oxidation resistivity, more compounds should be investigated. Especially metal hexaborides should be included because their octahedral boron framework represents an intermediate step between the planar boron sheets in metal diborides and the icosahedral boron polyhedra in MMB_{14} compounds. To obtain precise quantitative information about oxide layer thickness and also roughness and density, X-ray reflectometry with synchrotron radiation can be used. In this work, oxidation behavior of metal borides has been probed with XPS depth profiling by ion etching, which is an *ex situ* approach that has certain degrees of uncertainty. To gain a better understanding of the initial oxidation behavior and the resulting buildup of oxide layers, the very first steps of the oxidation process should be investigated. Molecular dynamics simulations based on density functional theory can provide predictions. XPS can be used to experimentally probe these predictions by performing *in situ* snapshot measurements of initially unoxidized samples being exposed to oxygen. Such experiments require a system with a leak valve, a very fast detector and preferably a heatable sample stage.

7. Acknowledgements

Special thanks to the Chair of Materials Chemistry, Prof. Dr. Jochen M. Schneider and Oliver Hunold, the supervisors of this thesis, as well as to Dr. Denis Music, Friederike Wittmers, Markus Momma, Philipp Keuter, Anna Lena Ravensburg and the rest of the team.

8. Appendix 1

This appendix provides information about the fitting procedures used to evaluate the XPS data. If not stated otherwise, synthetic peaks with mixed line 70% Gaussian – 30% Lorentzian line shapes were used and doublet pairs were constrained to have the same full width at half maximum (FWHM).

TiB_2 : The Ti 2p spectrum can be seen in **Figure 13**. Values of TiO_2 and TiB_2 were constrained to those taken from the first and last measurement cycle, respectively. 60% Lorentzian line shapes were

used for TiB_2 components. Other titanium oxides were fitted as suggested by *Biesinger et al.* [90], who used own measurements and values compiled from the NIST database. Different to *Biesinger et al.*, the 3/2 peak of Ti_2O_3 was chosen to be broader than the 1/2 peak, as this was also observed for TiO_2 and TiB_2 . The B 1s spectrum is shown in **Figure 14**. The B_2O_3 value from the NIST database is 193.2 (± 0.6) eV and was mostly measured for bulk samples. *Ong et al.* [56] measured a lower, fitting value of 192.4 eV for B_2O_3 present on surfaces and attributed the deviation to a negative fixed charged in the oxide. A rise of the binding energy of B_2O_3 with proceeding etch cycles indicates that this negative fixed charge was partially compensated by ion sputtering. *Ong et al.* identified an interfacial suboxide at

188.7 eV that was suggested to be B_6O . This suboxide is generally referred to B_6O in this work, for which NIST values scatter between 187.4 and 189.2 eV. All B 1s spectra have been fitted with the components mentioned above, therefore they are not described for the other compounds.

AlB₂: The Al 2s spectrum is shown in **Figure 15**. Al 2s and 2p values and FWHM of Al_2O_3 and AlB_2 were constrained to those taken from the first and last measurement cycle, respectively. Al 2s and 2p values of Al_2O_3 (119.2 and 74.4 eV) are in good agreement with NIST values (119.1 (± 1.3) and

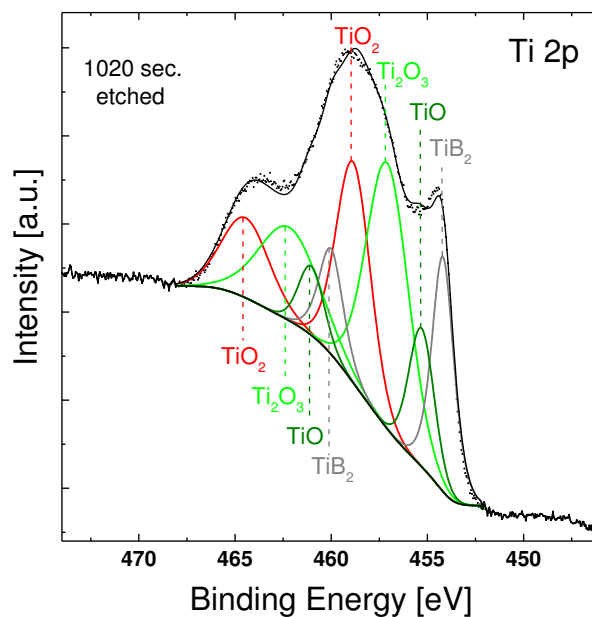


Figure 13: XPS Ti 2p spectrum of TiB_2

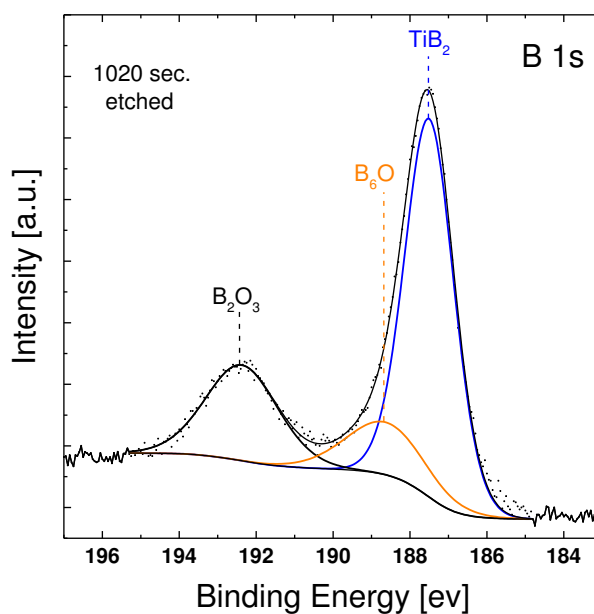


Figure 14: XPS B 1s spectrum of TiB_2

74.2 (± 0.8) eV). 70% and 50% Lorentzian line shapes were used for both 2s and 2p of Al_2O_3 peaks, respectively. The few reference values found for aluminum borates [91, 92] were too high to be fitted.

CaB₆: The Ca 2p spectrum is shown in **Figure 16**. The only component seen in the Ca 2p spectrum at the surface was attributed to a calcium borate. The 2p 3/2 NIST value for CaO (346.6 (± 0.5) eV) is too low to match. Ca 2p 3/2 and 1/2 values are 348.3 and 351.8 eV, respectively. In further measurement cycles, these values and according FWHM were used as constrains. No reliable reference values for calcium borates could be found. Another peak doublet that appeared after ion etching was attributed to CaB_6 . The binding energy values and FWHM were averaged over all measurements.

ZrYB₁₄: The B 1s and Zr 3d spectra are shown in **Figure 17**. Zr 3d values of ZrO_2 and ZrYB_{14} were constrained to those taken from the first and last measurement cycle, respectively. ZrO_2 3d 5/2 value (182.4 eV) is in good agreement with the NIST value (182.6 (± 0.6) eV). ZrO_2 peaks exhibit a broadening of about 1.7 eV after sputtering. This was not reported for ZrO_2 but does generally occur [82] and may be due to the presence of nanocrystalline stable cubic ZrO_2 . Another doublet at lower

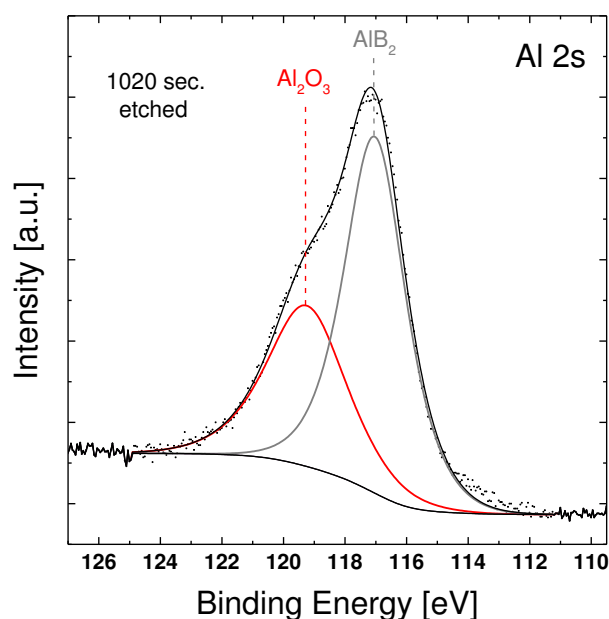


Figure 15: XPS Al 2s spectrum of AlB_2

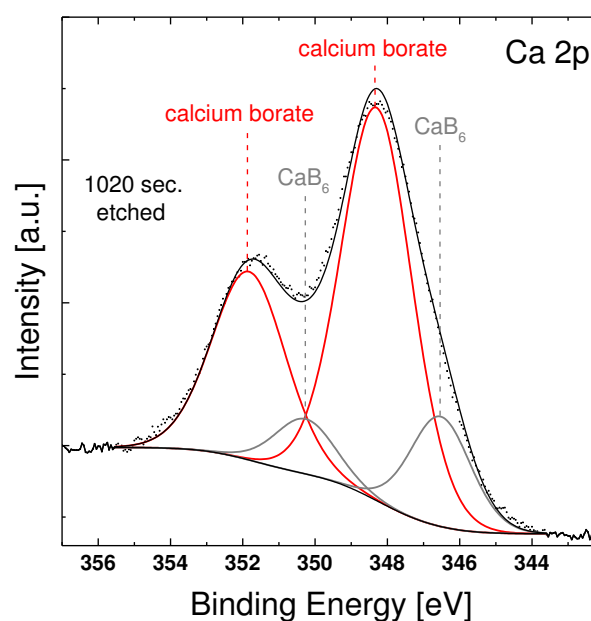


Figure 16: XPS Ca 2p spectrum of CaB_6

binding energy was observed at the surface that can be attributed to oxygen point defects, which were predicted for cubic ZrO_2 and also form by the substitution of Zr^{4+} cations with Y^{3+} [83]. Y 3d values of YBO_3 and ZrYB_{14} were constrained to those taken from the first and last measurement cycle, respectively (compare **Figure 18**). YBO_3 Y 3d 5/2 and 3/2 are 157.9 and 159.9 eV, respectively, which matches reported values of 158.0 and 160.0 eV [93] and a survey scan value of 159 eV [94]. Also yttrium hydroxide values match well for this component [95], but it is not likely that hydroxides would have formed at 700 °C or that they would endure several ion etching cycles, therefore they were not considered. Y_2O_3 and ZrYB_{14} have been regarded as one Y 3d doublet. The distinction is described in the

corresponding results and discussion paragraph. The Y 3d component at higher binding energy is ascribed to a higher borate, matching values for $\text{YAl}_3(\text{BO}_3)_4$ were reported [93], but also other borates might be suitable.

AlYB_{14} : **Figure 18** shows the Y 3d spectrum of AlYB_{14} . The Y 3d region was fitted in the same way as for ZrYB_{14} . The Al 2s peak had a bad signal to noise ratio and did not obviously exhibit different components. The presence of Al_2O_3 seemed likely, using the corresponding binding energy

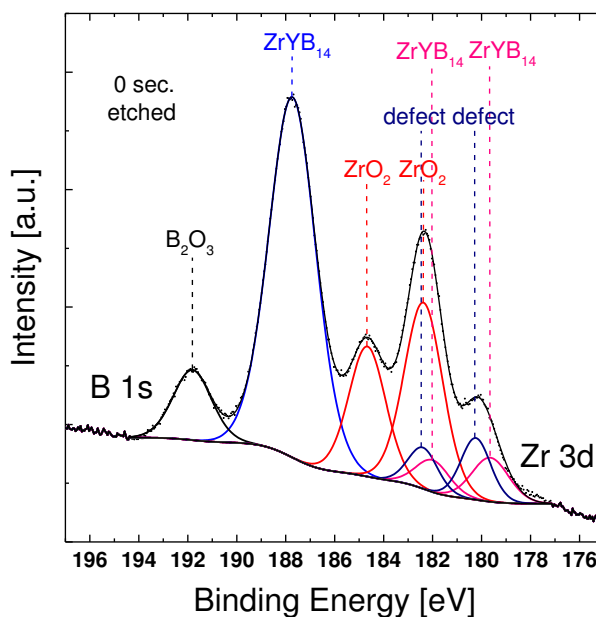


Figure 17: XPS B 1s and Zr 3d spectra of ZrYB_{14}

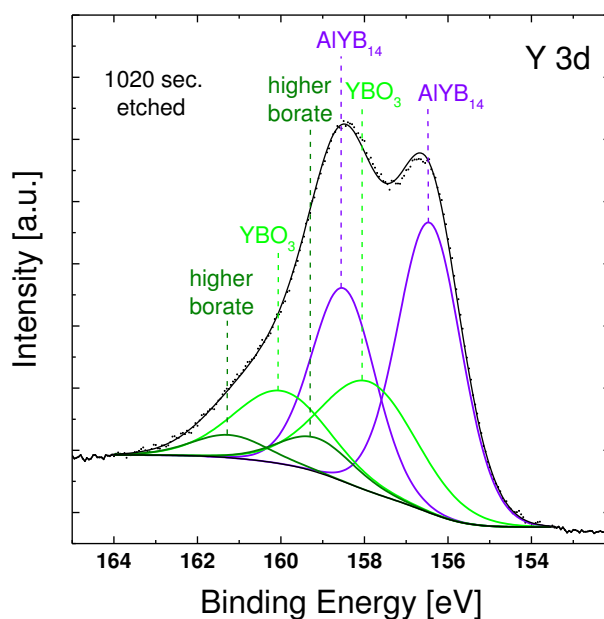


Figure 18: XPS Y 3d spectrum of AlYB_{14}

and FWHM measured for AlB_2 . The only other component fitted into the peak was ascribed to AlYB_{14} , but it is at unusually high binding energy compared to AlB_2 (118.6 and 117.1 eV, respectively). Reference values found for yttrium aluminates [96, 97] did not match, however the presence of other oxides or borates cannot certainly be excluded.

YB_6 : The Y 3d region was fitted similarly to ZrYB_{14} and AlYB_{14} (compare **Figure 18**). YBO_3 and YB_6 , but no higher borate components, were observed. In contrast to ZrYB_{14} and AlYB_{14} , YB_6 peaks were broader than those of YBO_3 .

MgB_2 : The Mg 2p spectrum is shown in **Figure 19**. The MgO 2p value of 50.2 eV is a little lower than the NIST value of 50.79 (± 0.33). The presence of magnesium borates cannot be excluded, but no reference values were found. Hence, the deconvolution might not be accurate.

VB_2 : The V 2p spectrum is shown in **Figure 20**. All vanadium oxides were fitted as suggested by *Biesinger et al.* [90], using same FWHM for doublet pairs. The 1/2 peak of VB_2 is slightly broader than the 3/2 peak.

ZrB_2 : The Zr 3d and B 1s spectra are shown in **Figure 21**. ZrO_2 Zr 3d values were those also used for ZrYB_{14} . The Zr 3d 5/2 value of Zr(OH)_4 was constrained to the reported value of 183.6 eV [98]

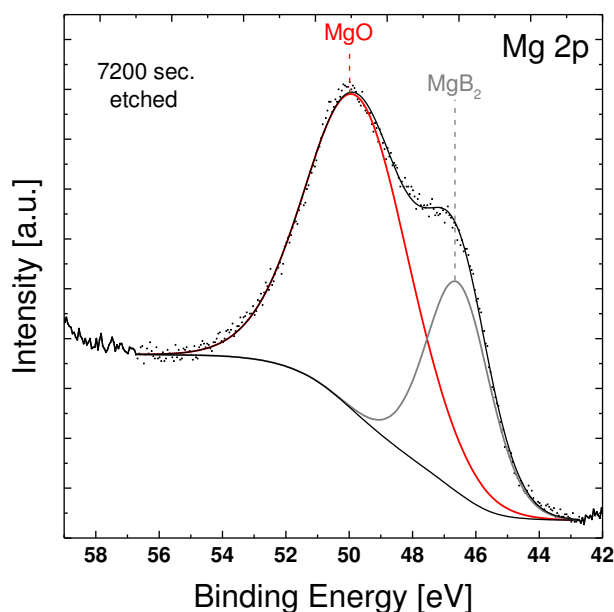


Figure 19: XPS Mg 2p spectrum of MgB_2

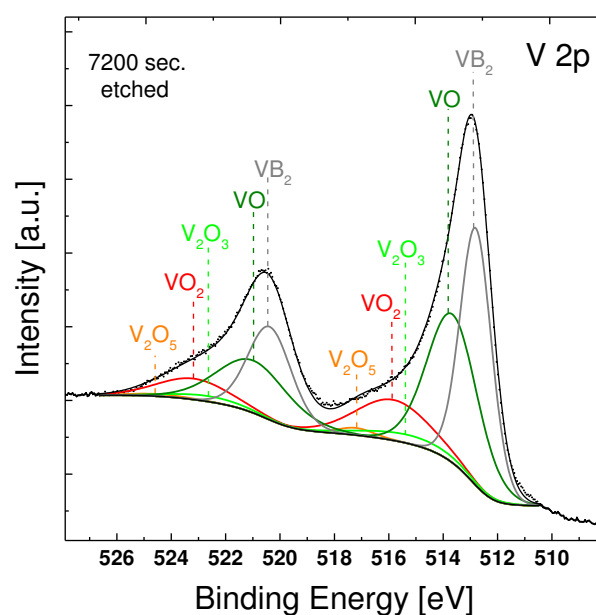


Figure 20: XPS V 2p spectrum of VB_2

and the spin-orbit splitting was constrained to be the same as for ZrO_2 . It is noteworthy that no boron suboxide (B_6O) occurred neither on the powder nor the sintered sample.

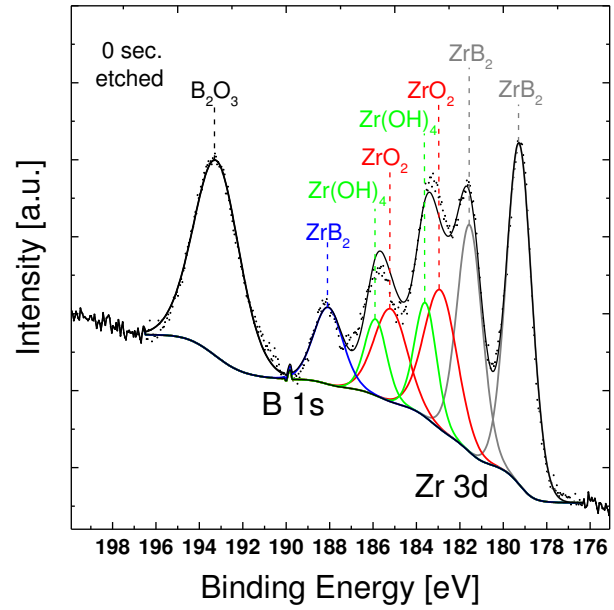


Figure 21: XPS B 1s and Zr 3d spectra of ZrB_2

9. Appendix 2

This appendix describes the model used by *Mathieu et al.* to calculate oxide layer thickness from XPS data [86-88].

The intensity I_A of emitted electrons for a given transition A is given by

$$I_A = K \int_0^\infty C_A(z) \exp(-z/\Lambda) dz \quad (1)$$

where $C_A(z)$ is the atomic concentration of element A, which is a function of depth z and Λ is the electron escape depth given by

$$\Lambda = \lambda \cos \phi \quad (2)$$

where λ is the inelastic mean free path of a photoelectron in a given matrix and ϕ is the take-off angle with respect to the surface normal. K is a constant depending on instrumental factors. Assuming a step-like coverage by a uniform oxide layer, one obtains by integration of (1) for the intensity of photoelectrons for a transition A

$$I_{A,oxide} = K C_{A,oxide} \Lambda_{A,oxide} (1 - \exp(-l/\Lambda_{A,oxide})) \quad (3)$$

where l is the thickness of the oxide layer and $\Lambda_{A,oxide}$ is the electron escape depth in the oxide. By integration for the intensity of photoelectrons from the underlying substrate compound, one obtains

$$I_{A,sub} = K C_{A,sub} \Lambda_{A,sub} \exp(-l/\Lambda_{A,oxide}) \quad (4)$$

The ratio of intensities ((3) and (4)) is independent of instrumental factors:

$$\frac{I_{A,sub}}{I_{A,oxide}} = R^* \frac{\exp(-l/\Lambda_{A,oxide})}{1-\exp(-l/\Lambda_{A,oxide})} \quad (5)$$

with

$$R^* = \frac{C_{A,sub}\lambda_{A,sub}\cos\phi}{C_{A,oxide}\lambda_{A,oxide}\cos\phi} \quad (6)$$

Transposing (5) for the thickness l gives

$$l = -\lambda_{A,oxide} \cos\phi \ln \left(\frac{\frac{I_{A,sub}}{I_{A,oxide}}}{\frac{I_{A,sub}}{I_{A,oxide}} + R^*} \right) \quad (7)$$

The electron take-off angle was 0° during all measurements, therefore $\cos\phi = 1$. Atomic concentrations have been calculated according to $C = \frac{\rho}{M}$ where ρ and M are density and molecular weight, respectively. Densities were taken from the Springer Materials Linus Pauling File database [99]. Inelastic mean free paths for electrons in inorganic compounds were calculated according to *Seah and Dench* [100]:

$$\lambda_A = 0.72 a_A^{1.5} E_A^{0.5} \quad (8)$$

where E_A is the kinetic energy of a photoelectron from a transition A and a_A is the monolayer thickness in nanometers of the compound given by

$$a^3 = \frac{M}{\rho n N} * 10^{21} \quad (9)$$

where N is Avogadro's number and n is the total number of atoms per molecule. **Table 2** shows λ and a values calculated with (8) and (9).

Transition / Substrate Compound / Oxide	a_{sub} [nm]	a_{oxide} [nm]	$\lambda_{A,sub}$ [nm]	$\lambda_{A,oxide}$ [nm]
Al 2s / Al _{0.76} Y _{0.98} B ₁₄ / Al ₂ O ₃	0.207	0.204	2.504	2.453
Y 3d 5/2 / Al _{0.76} Y _{0.98} B ₁₄ / YBO ₃	0.207	0.222	2.469	2.740
B 1s / Al _{0.76} Y _{0.98} B ₁₄ / B ₂ O ₃	0.207	0.209	2.440	2.467
Zr 3d 5/2 / Zr _{0.45} Y _{0.47} B ₁₄ / ZrO ₂	0.190	0.233	2.155	2.928
Y 3d 5/2 / Zr _{0.45} Y _{0.47} B ₁₄ / YBO ₃	0.190	0.222	2.174	2.740
B 1s / Zr _{0.45} Y _{0.47} B ₁₄ / B ₂ O ₃	0.190	0.209	2.148	2.467
Ti 2p 3/2 / Ti _{0.5} B ₂ / TiO ₂	0.177	0.218	1.720	2.357
B 1s / Ti _{0.5} B ₂ / B ₂ O ₃	0.177	0.209	1.930	2.466
Al 2s / AlB ₂ / Al ₂ O ₃	0.190	0.204	2.144	2.467
B 1s / AlB ₂ / B ₂ O ₃	0.190	0.209	2.201	2.453
Ca 2p 3/2 / CaB ₆ / CaB ₄ O ₇	0.217	0.216	2.445	2.435
B 1s / CaB ₆ / B ₂ O ₃	0.217	0.209	2.615	2.466

Table 2: Physical parameters for thickness analysis

Declaration of Originality

I confirm that, unless stated otherwise, this work is the result of my own efforts. These efforts include the originality of written works as well as diagrams or similar pictorial material and results.

Where material is drawn from elsewhere, references are included.

(Pascal Bliem)

10. References

1. G.P. Shveikin and A.L. Ivanovskii, Russian Chemical Reviews, 1994. **63**(9): p. 711 - 734.
2. A. Passerone, F. Valenza, and M.L. Muolo, Journal of Materials Science, 2012. **47**(24): p. 8275-8289.
3. M. Elfström, Acta Chemica Scandinavica, 1961. **15**(5): p. 1178.
4. M. Wittmer, Journal of Vacuum Science & Technology A: Vacuum, Surfaces, and Films, 1984. **2**(2): p. 273.
5. W.S. Williams, Journal of Metals, 1997. **49**(3): p. 38-42.
6. G. Mavel, J. Escard, P. Costa, and J. Castaing, Surface Science, 1973. **35**: p. 109-116.

7. V.V. Odintsov and S.N. Yakovenko, *Soviet Powder Metallurgy and Metal Ceramics*, 1984. **23**.
8. J.F. Watts and J. Wolstenholme, *An Introduction To Surface Analysis by XPS and Aes*. 2003.
9. B. Callmer, L.-E. Tergenius, and J.O. Thomas, *Journal of Solid State Chemistry*, 1978. **26**: p. 275-279.
10. R.B. King, *Chemical Reviews*, 2001. **101**: p. 1119-1152.
11. W.N. Lipscomb and D. Britton, *The Journal of Chemical Physics*, 1960. **33**(1): p. 275.
12. B. Post and F.W. Glaser, *The Journal of Chemical Physics*, 1952. **20**(6): p. 1050-1051.
13. F.W. Glaser, D. Moskowitz, and B. Post, *Journal of Metals*, 1953. **5**(9): p. 1119-1120.
14. B. Aronsson, E. Stenberg, and J. Aselius, *Nature*, 1962. **195**(4839): p. 377.
15. P. Rogl, H. Nowotny, and F. Benesovsky, *Monatsh. Chem.*, 1971. **102** p. 678.
16. B. Aronsson, E. Stenberg, and J. Aselius, *Acta Chemica Scandinavica*, 1960. **14**(3): p. 733-741.
17. Y. Wang, W. Chen, X. Chen, H.Y. Liu, Z.H. Ding, Y.M. Ma, X.D. Wang, Q.P. Cao, and J.Z. Jiang, *Journal of Alloys and Compounds*, 2012. **538**: p. 115-124.
18. Y. Pan, *Computational Materials Science*, 2014. **92**: p. 57-62.
19. J.K. Burdett, E. Canadell, and G.J. Miller, *Journal of the American Chemical Society*, 1986. **108**: p. 6561-6568.
20. C. Ying, E. Zhao, L. Lin, and Q. Hou, *Modern Physics Letters B*, 2014. **28**(27).
21. D. Emin, *Journal of Solid State Chemistry*, 2006. **179**(9): p. 2791-2798.
22. Andersso.S and Lundstro.T, *Acta Chemica Scandinavica*, 1968. **22**(10): p. 3103.
23. H.Y. Niu, J.Q. Wang, X.Q. Chen, D.Z. Li, Y.Y. Li, P. Lazar, R. Podloucky, and A.N. Kolmogorov, *Physical Review B*, 2012. **85**(14).
24. H.Y. Gou, N. Dubrovinskaia, E. Bykova, A.A. Tsirlin, D. Kasinathan, W. Schnelle, A. Richter, M. Merlini, M. Hanfland, A.M. Abakumov, D. Batuk, G. Van Tendeloo, Y. Nakajima, A.N. Kolmogorov, and L. Dubrovinsky, *Physical Review Letters*, 2013. **111**(15).
25. M. Yang, Y.C. Wang, J.L. Yao, Z.P. Li, J. Zhang, L.L. Wu, H. Li, J.W. Zhang, and H.Y. Gou, *Journal of Solid State Chemistry*, 2014. **213**: p. 52-56.
26. M. Wang, Y.W. Li, T. Cui, Y.M. Ma, and G.T. Zou, *Applied Physics Letters*, 2008. **93**(10).
27. M. Aono, S. Kawai, S. Kono, M. Okusawa, T. Sagawa, and Y. Takehana, *Journal of Physics and Chemistry of Solids*, 1976. **37**: p. 215-219.
28. H. Werheit, V. Filipov, K. Shirai, H. Dekura, N. Shitsevalova, U. Schwarz, and M. Armbruster, *Journal of Physics: Condensed Matter*, 2011. **23**(6): p. 065403.
29. I. Higashi, *Journal of Solid State Chemistry*, 2000. **154**(1): p. 168-176.
30. H. Kolpin, D. Music, G. Henkelman, J. Emmerlich, F. Munnik, and J.M. Schneider, *Journal of Physics: Condensed Matter*, 2009. **21**(35): p. 355006.
31. I. Higashi, M. Kobayashi, S. Okada, K. Hamano, and T. Lundström, *Journal of Crystal Growth*, 1993. **128**: p. 1113-1119.
32. L. Scatteia, G. Tomasetti, G. Rufolo, F. De Filippis, and G. Marino, *Space technology and applications. Intern Forum STAIF7*, 2005. **46**(129).
33. J. Sung, D.M. Goedde, G.S. Girolami, and J.R. Abelson, *Journal of Applied Physics*, 2002. **91**(6): p. 3904-3911.
34. Z.J. Jin, M. Zhang, D.M. Guo, and R.K. Kang, *Key Engineering Materials*, 2005. **291-292**: p. 537-542.
35. S.Z. Jin, H.L. Zhang, S.S. Jia, and J.F. Li, *Materials Science Forum*, 2005. **475-479**: p. 1555-1558.
36. L. Huerta, A. Durán, R. Falconi, M. Flores, and R. Escamilla, *Physica C: Superconductivity*, 2010. **470**(9-10): p. 456-460.
37. A. Tampieri and A. Bellosi, *Journal of Materials Science*, 1993. **28**: p. 649-653.
38. A. Agarwal, L.R. Katipelli, and N.B. Dahotre, *Metallurgical and Materials Transactions A*, 2000. **31**: p. 461-473.
39. A. Kulpa and T. Troczynski, *Journal of the American Ceramic Society*, 1996. **79**(2): p. 518-520.
40. M.L. Whittaker, H.Y. Sohn, and R.A. Cutler, *Journal of Solid State Chemistry*, 2013. **207**: p. 163-169.
41. J.-I. Matsushita, K. Mori, Y. Nishi, and Y. Sawada, *Journal of Materials Synthesis and Processing*, 1998. **6**(6): p. 407-410.

42. J.-I. Matsushita and S. Komarneni, *Journal of Materials Science*, 1999. **34**: p. 3043 – 3046.
43. National Institute of Standards and Technology, *NIST X-ray Photoelectron Spectroscopy Database, Version 4.1*. 2012.
44. K. Sarakinos, J. Alami, and S. Konstantinidis, *Surface and Coatings Technology*, 2010. **204**(11): p. 1661-1684.
45. R. Telle, *Vorlesungsmanuskript „Nichtmetallische Werkstoffe: Keramik“*, Institut für Gesteinshüttenkunde, RWTH Aachen, Selbstverlag; 3. Auflage, . 2007.
46. A.R. Clarke and C.N. Eberhardt, *Microscopy techniques for materials science*. 2002: Woodhead Publishing.
47. S. Richter, *Grundlagen und Anwendungen in der Elektronenstrahlmikroanalyse*.
48. G. Gottstein, *Materialwissenschaften und Werkstofftechnik 4. Auflage* 2014.
49. P.W. Atkins and J. de Paula, *Physikalische Chemie 5. Auflage* 2013.
50. C. Genzel, *Physica Status Solidi (a)*, 1997. **159**(2): p. 283-296.
51. P. Swift, *Surface and Interface Analysis*, 1982. **4**(2): p. 47-51.
52. J.H. Scofield, *Journal of Electron Spectroscopy and Related Phenomena*, 1976. **8**: p. 129-137.
53. D. Music, F. Hensling, T. Pazur, J. Bednarcik, M. Hans, V. Schnabel, C. Hostert, and J.M. Schneider, *Solid State Communications*, 2013. **169**: p. 6-9.
54. L. Shi, Y. Gu, L. Chen, Z. Yang, J. Ma, and Y. Qian, *Chemistry Letters*, 2003. **32**(10): p. 958-959.
55. L. Zhang, G. Feng, and G. Min, *Journal of Nanoscience and Nanotechnology*, 2014. **14**(10): p. 8083-8086.
56. C.W. Ong, *Journal of Applied Physics*, 2004. **95**(7): p. 3527.
57. J.P. Rivière, S. Miguet, M. Cahoreau, J. Chaumont, and J. Delafond, *Surface and Coatings Technology*, 1996. **84**: p. 398-403.
58. F.V.E. Hensling, *Bachelor of Science Thesis: Structure and mechanical properties of Y-Al-B thin films synthesized by HPPMS*. 2013.
59. B. Timmermans, N. Vaeck, A. Hubin, and F. Reniers, *Surface and Interface Analysis*, 2002. **34**(1): p. 356-359.
60. R.P. Vasquez, C.U. Jung, M.S. Park, H.J. Kim, J.Y. Kim, and S.I. Lee, *Preprint Condensed Matter*, 2001.
61. A. Serquis, Y.T. Zhu, D.E. Peterson, F.M. Mueller, R.K. Schulze, V.F. Nesterenko, and S.S. Indrakanti, *Applied Physics Letters*, 2002. **80**(23): p. 4401.
62. E.Z. Kurmaev, I.I. Lyakhovskaya, J. Kortus, A. Moewes, N. Miyata, M. Demeter, M. Neumann, M. Yanagihara, M. Watanabe, T. Muranaka, and J. Akimitsu, *Physical Review B*, 2002. **65**(13).
63. L. Petaccia, C. Cepek, S. Lizzit, R. Larciprete, R. Macovez, M. Sancrotti, and A. Goldoni, *New Journal of Physics*, 2006. **8**: p. 12-12.
64. S.-F. Wang, Y.-L. Zhou, Y.-B. Zhu, Q. Zhang, K. Xie, Z.-H. Chen, H.-B. Lu, and G.-Z. Yang, *Chinese Physics*, 2002. **11**(12): p. 1300-03.
65. A.T. Matveev, J. Albrecht, M. Konuma, G. Cristiani, Y. Krockenberger, U. Starke, G. Schütz, and H.U. Habermeier, *Superconductor Science and Technology*, 2006. **19**(4): p. 299-305.
66. A. Santoni, U.B. Vetrella, G. Celentano, U. Gambardella, and A. Mancini, *Applied Physics A*, 2006. **86**(4): p. 485-490.
67. S. Sen, D.K. Kaswal, A. Singh, T.V. Chandrasekhar Rao, K.P. Muthe, J.C. Vyas, L.C. Gupta, S.K. Gupta, and V.C. Sahni, *Pramana Journal of Physics*, 2002. **58**(5 & 6): p. 867–870.
68. J. Vleugels, B. Basu, K.C. Hari Kumar, R.G. Vitchev, and O. Van der Biest, *Metallurgical and Materials Transactions A*, 2002. **33**(12): p. 3847-3859.
69. R. Ranjit, W. Zagodzón-Wosik, I. Rusakova, P. Van der Heide, Z.H. Zhang, J. Bennett, and D. Marton, *Reviews on Advanced Material Science*, 2004. **8**: p. 176-184.
70. J.H. Liu, B. Blanpain, and P. Wollants, *Key Engineering Materials*, 2008. **368-372**: p. 1347-1350.
71. C.S. Choi, G.A. Ruggles, C.M. Osburn, and G.C. Xing, *Journal of the Electrochemical Society*, 1991. **138**(10): p. 3053-3061.
72. J. Stuart, A. Hohenadel, X. Li, H. Xiao, J. Parkey, C.P. Rhodes, and S. Licht, *Journal of the Electrochemical Society*, 2014. **162**(1): p. A192-A197.

73. L. Shi, Y. Gu, L. Chen, Z. Yang, J. Ma, and Y. Qian, *Materials Letters*, 2004. **58**(22-23): p. 2890-2892.
74. R. Singh, *Surface Science Spectra*, 2000. **7**(4): p. 310.
75. M. Brochu, B.D. Gauntt, L. Boyer, and R.E. Loehman, *Journal of the European Ceramic Society*, 2009. **29**(8): p. 1493-1499.
76. S.-H. Lee, Y. Sakka, and Y. Kagawa, *Journal of the American Ceramic Society*, 2008. **91**(5): p. 1715-1717.
77. J.F. Pierson, J.F. Belmonte, and H. Michel, *Applied Surface Science*, 2001. **172**: p. 285-294.
78. R. Armitage, J. Suda, and T. Kimoto, *Surface Science*, 2006. **600**(7): p. 1439-1449.
79. D.M. Stewart, D.J. Frankel, and R.J. Lad, *Journal of Vacuum Science & Technology A: Vacuum, Surfaces, and Films*, 2015. **33**(3): p. 031505.
80. G. Zhao, X. Zhang, Z. Shen, D. Zhang, C. Hong, J. Li, Z. Zhang, and B. Fahrenholtz, *Journal of the American Ceramic Society*, 2014. **97**(8): p. 2360-2363.
81. L. Chen, Y. Gu, Z. Yang, L. Shi, J. Ma, and Y. Qian, *Scripta Materialia*, 2004. **50**(7): p. 959-961.
82. S. Hashimoto, A. Tanaka, A. Murata, and T. Sakurada, *Surface Science*, 2004. **556**(1): p. 22-32.
83. B. Liu, H. Xiao, Y. Zhang, D.S. Aidhy, and W.J. Weber, *Computational Materials Science*, 2014. **92**: p. 22-27.
84. W.F. Bradley, D.L. Graf, and R.S. Roth, *Acta Crystallographica*, 1966. **20**: p. 283-287.
85. S.G.T.E., *Landolt-Börnstein Thermodynamic Properties of Inorganic Materials*. 2006. **Group IV Volume 19**(Subvolume B Part 4).
86. H.J. Mathieu, *Journal of Vacuum Science & Technology A: Vacuum, Surfaces, and Films*, 1985. **3**(2): p. 331.
87. H.J. Mathieu and D. Landolt, *Surface and Interface Analysis*, 1984. **6**(2): p. 82-89.
88. H.J. Mathieu and D. Landolt, *Oberfläche/Surface*, 1980. **21**: p. 8.
89. K.R. Lawless, *Reports on Progress in Physics*, 1974. **37**: p. 231-316.
90. M.C. Biesinger, L.W.M. Lau, A.R. Gerson, and R.S.C. Smart, *Applied Surface Science*, 2010. **257**(3): p. 887-898.
91. H.S. Song, J. Zhang, J. Lin, S.J. Liu, J.J. Luo, Y. Huang, E.M. Elssfah, A. Elsanousi, X.X. Ding, J.M. Gao, and C. Tang, *Journal of Physical Chemistry C*, 2007. **111**: p. 1136-1139.
92. J. Hu, X.H. Zhao, S.W. Tang, and M.R. Sun, *Surface and Coatings Technology*, 2006. **201**(6): p. 3814-3818.
93. H. Deters, A.S.S. de Camargo, C.N. Santos, C.R. Ferrari, A.C. Hernandez, A. Ibanez, M.T. Rinke, and H. Eckert, *Journal of Physical Chemistry C*, 2009. **113**: p. 16216-16225.
94. H. Zhu, L. Zhang, T. Zuo, X. Gu, Z. Wang, L. Zhu, and K. Yao, *Applied Surface Science*, 2008. **254**(20): p. 6362-6365.
95. D. Majumdar and D. Chatterjee, *Journal of Applied Physics*, 1991. **70**(2): p. 988.
96. K. Matsunouchi, N. Komatsu, C. Kimura, H. Aoki, and T. Sugino, *Applied Surface Science*, 2009. **255**(9): p. 5021-5024.
97. D.A. Pawlak, K. Wozniak, Z. Frukacz, T.L. Barr, D. Fiorentino, and S. Hardcastle, *Journal of Physical Chemistry B*, 1999. **103**: p. 3332-3336.
98. T.L. Barr, *Journal of Physical Chemistry*, 1978. **82**(16): p. 1801-1810.
99. (MPDS), *LINUS PAULING FILE Multinaries Edition – 2012*. 2014.
100. M.P. Seah and W.A. Dench, *Surface and Interface Analysis*, 1979. **1**(1): p. 2-11.